

Secondary instability of wall-bounded shear flows

By STEVEN A. ORSZAG AND ANTHONY T. PATERA

Massachusetts Institute of Technology, Cambridge, MA 02139

(Received 19 January 1982 and in revised form 13 September 1982)

An analysis is given of a secondary instability that obtains in a wide class of wall-bounded parallel shear flows, including plane Poiseuille flow, plane Couette flow, flat-plate boundary layers, and pipe Poiseuille flow. In these flows it is shown that two-dimensional finite-amplitude waves are (exponentially) unstable to infinitesimal three-dimensional disturbances. This secondary instability seems to be the prototype of transitional instability in these flows in that it has the characteristic (convective) timescales observed in the typical transitions. In the case of plane Poiseuille flow, two-dimensional nonlinear equilibria and quasi-equilibria exist, and the stability of the secondary flow is determined by a three-dimensional linear eigenvalue calculation. In flows without equilibria (e.g. pipe flow), a time-dependent stability analysis is performed by direct spectral numerical calculation of the incompressible three-dimensional Navier–Stokes equations.

The energetics and vorticity dynamics of the instability are discussed. It is shown that the two-dimensional wave mediates the transfer of energy from the mean flow to the three-dimensional perturbation but does not directly provide energy to the disturbance. The instability is of an inviscid character as it persists to high Reynolds numbers and grows on convective timescales. Maximum vorticity (inflexion-point) arguments predict some features of the instability like phase-locking of the two-dimensional and three-dimensional waves, but they do not explain its essential three-dimensionality. The inviscid vorticity dynamics of the instability shows that vorticity-stretching and tilting effects are both required to explain the persistent exponential growth. The instability is not centrifugal in nature.

The three-dimensional instability requires that a threshold two-dimensional amplitude be achieved (about 1% of the centreline velocity in plane Poiseuille flow): the growth rates are relatively insensitive to amplitude for moderate two-dimensional amplitudes. With moderate two-dimensional amplitudes, the critical Reynolds numbers for substantial three-dimensional growth are about 1000 in plane Poiseuille and Couette flows and several thousand in pipe Poiseuille flow. The asymptotic (as R approaches infinity) growth rate in plane Poiseuille flow is approximately $0.15h/U_0$, where h is the half-channel width and U_0 is the centreline velocity.

It is possible to make some progress identifying experimental features of transitional spot structure with aspects of the nonlinear two-dimensional/linear three-dimensional instability. The principal excitation of the eigenfunction of the three-dimensional (growing) disturbance is localized within a given periodicity length (in both the stream and cross-stream directions) near the vorticity maxima of the two-dimensional flow; its planwise structure corresponds to that of observed streaks in early transitional spots; its vortical structure resembles that of a streamwise vortex lifting off the wall. As the three-dimensional disturbance grows to finite amplitude, the flows become chaotic with statistical structure similar to that observed experimentally in moderate-Reynolds-number turbulent shear flows.

1. Introduction

The process by which a laminar shear flow undergoes transition to turbulence is of fundamental fluid-dynamical interest. In this paper, we address this question from the viewpoint of stability theory. In particular, we shall isolate an apparently universal secondary instability that obtains in wall-bounded shear flows and seems to explain the dominant features of the initial transition process in these flows.

Recent research has emphasized the diverse routes by which a flow may become turbulent. On the one hand, there are flows like Bénard convection (Gollub & Benson 1980; McLaughlin & Orszag 1982) and Taylor–Couette flow (Gorman, Reith & Swinney 1980) in which a sequence of ordered transitions may be discerned. In these flows, increasing Reynolds number may bring on chaos after three incommensurate bifurcations (Ruelle & Takens 1971), after infinitely many period-doubling bifurcations (Feigenbaum 1980), or intermittently (Manneville & Pomeau 1980). The choice of which, if any, of these three scenarios of transition occur seems to be dependent on geometry, initial conditions, and other specific features of the flows. This sensitivity to detail is perhaps due to the comparatively low Reynolds numbers at which weak chaos first appears in these flows.

On the other hand, laboratory experiments (Carlson, Widnall & Peeters 1981) and numerical simulations (Orszag & Kells 1980) indicate that, in wall-bounded shear flows, the transition to turbulence is violent in the sense that the flow ‘snaps’ from a laminar state to a strongly chaotic state with apparently no intervening bifurcations to another stable solution. In snap-through transitions, the stability characteristics of the mean flow largely determine the early stages of the transition process and perhaps the final turbulent flow.

The instability process to be examined involves essentially three steps:

- (i) primary (linear) instability of the basic shear flow;
- (ii) nonlinear saturation of the primary instability and formation of a secondary flow;
- (iii) secondary instability, i.e. linear instability of the secondary flow.

Classical hydrodynamical stability theory (Lin 1955; Drazin & Reid 1981) addresses step (i), while the standard techniques of nonlinear stability theory (Stuart 1960; Drazin & Reid 1981) address step (ii). The bulk of this paper addresses step (iii). In many cases, the first step or even the first two steps may be absent or unobservable in practice, so it may seem bootless to analyse step (iii). However, as discussed further below, the sequence (i)–(iii) provides a rational framework in which to understand the physics of instabilities leading to chaos and turbulence.

The primary/secondary instabilities discussed here are distinguished by the fact that the primary instability is restricted to be two-dimensional while the secondary instability is allowed to be three-dimensional. In plane parallel flows, Squires’ (1933) theorem justifies the two-dimensional form of the primary instability; in other parallel flows, two-dimensionality (axisymmetry) is assumed. It will be shown that the two-dimensional primary instability leads to a nonlinear periodic flow while secondary instability likely leads to chaotic behaviour. The three-dimensional character of secondary instability is consistent with the idea that turbulence is intrinsically three-dimensional. The important question as to whether the secondary instability results in a tertiary ordered state or a chaotic regime will not be considered in great detail here, although a first essay in this direction will be given in §7.

Choosing the primary instabilities to be three-dimensional rather than two-dimensional would complicate the analysis of the secondary instability process. In

particular, general three-dimensional modes do not appear to saturate in ordered states in shear flows such as plane Poiseuille flow (Orszag & Kells 1980). This might suggest considering three-dimensional primary instability rather than the sequence of events (i)–(iii) enumerated above. The point is that, while three-dimensional primary instabilities may eventually lead to chaos, they by no means solve the transition problem, as the time and space scales of the instability bear no resemblance to experimentally observed transitions. On the other hand, as we shall see below, the secondary instabilities arising in step (iii) do have features that qualify them as transitional instabilities. First, secondary instability is inherently three-dimensional and has ‘explosive’ (convective) growth rates, as opposed to the diffusive growth rates of primary exponential instability. Secondly, the instability obtains at Reynolds numbers like those observed at the onset of transition. For these reasons, we believe that the three-dimensional secondary-instability process to be studied here is in fact the right framework in which to make a systematic deterministic analysis of a flow undergoing an explosive transition to turbulence. Another reason for studying secondary instability as described by the three steps listed above is that this scenario is similar to that of the instability process found experimentally in the forced transition experiments of Klebanoff, Tidstrom & Sargent (1962), Nishioka, Iida & Ichikawa (1975), Nishioka, Iida & Kanbayashi (1978) in boundary layers and plane Poiseuille flow respectively. Although quantitative comparisons of Klebanoff’s ‘peak–valley’ splitting with the secondary instability to be presented below may certainly be fruitful, we will not make these comparisons here (but see the recent work of Kleiser & Schumann 1983). Such comparisons (at least in the later stages of transition) would best be done using inflow/outflow calculations. Even in the early stages of transition, great care must be taken in interpreting the experimental results, as will be briefly demonstrated in §4.

The idea that secondary three-dimensional instability of states induced by primary (two-dimensional) instabilities may be a prototype of a transitional instability has been discussed by us before (Orszag & Kells 1980; Orszag & Patera 1980, 1981*a*). In this paper we emphasize the physical properties of this instability and its apparently universal character in wall-bounded shear flows. Its universal character in free-shear flows is discussed by Brachet & Orszag (1983).

In §2 the primary linear instabilities of wall-bounded shear flows are discussed. Two canonical cases are emphasized: flow in a channel and in a pipe driven by a pressure gradient, i.e. plane Poiseuille flow and pipe Poiseuille flow respectively. In §3 the nonlinear saturation process of the primary instability is discussed. In §4 the concept of linear secondary instability is introduced and applied to the canonical Poiseuille flows. In §5 the structure and dynamics of the secondary instability are analysed. Then, in §6 the theory is applied to other shear flows, namely plane Couette flow and the boundary layer over a flat plate. Finally, in §7 the extent to which the secondary instability introduced here relates to the actual transition process is examined. It is only at this point that fully nonlinear three-dimensional interaction is included. In the appendices, some technical details of our methods are given.

2. Primary instability

Shear flows can be divided into three groups according to their linear stability characteristics. The first group, characterized by having inflexional mean-velocity profiles, includes those flows that are inviscidly unstable to infinitesimal disturbances. In fact, wall-bounded shear flows found in nature are typically not inflexional so this

case will not be considered here. The second group consists of flows that are inviscidly linearly stable, but can be unstable to infinitesimal viscous disturbances. Two examples of such flows are plane Poiseuille flow and Blasius (flat-plate boundary-layer) flow. Both these flows have finite (linear) critical Reynolds numbers but, since their instability is driven by viscosity, the flows are stable to disturbances of fixed wavenumber at sufficiently high Reynolds number. The third group includes flows that are linearly stable to all infinitesimal disturbances. Prototypes are pipe Poiseuille flow (Salwen, Cotton & Grosch 1980; Davey & Drazin 1969; Metcalfe & Orszag 1973) and plane Couette flow (Davey 1973).

In linear stability analyses of planar shear flows the velocity field is assumed to be of the form

$$\mathbf{v} = U_{\parallel}(z) \hat{\mathbf{x}} + \epsilon \operatorname{Re} \{ \mathbf{v}'(z) e^{i(\alpha x + \beta y - \omega t)} \} \quad (\epsilon \ll 1), \quad (2.1)$$

where x , y and z (u , v and w) are the streamwise, spanwise and cross-stream directions (velocities) respectively. Here U_{\parallel} is the parallel laminar basic flow (in the streamwise direction), and \mathbf{v}' is the perturbation. The streamwise and spanwise wavenumbers are α and β respectively. Flow quantities are non-dimensionalized with respect to a length h (channel half-width, pipe radius or boundary-layer thickness) and a velocity U_0 (centreline or freestream); the resulting Reynolds number is $R = U_0 h/\nu$, where ν is the kinematic viscosity of the fluid.

The equations of linear theory are obtained by inserting (2.1) into the incompressible Navier–Stokes equations (here given for plane Poiseuille flow),

$$\frac{\partial \mathbf{v}}{\partial t} + (\mathbf{v} \cdot \nabla) \mathbf{v} = -\nabla p + \frac{2}{R} \hat{\mathbf{x}} + \frac{1}{R} \nabla^2 \mathbf{v}, \quad (2.2)$$

$$\nabla \cdot \mathbf{v} = 0, \quad (2.3)$$

and linearizing with respect to ϵ . Note that the total pressure is $p - (2/R)x$. The boundary conditions on (2.2) are

$$\mathbf{v}(x, y, z = \pm 1, t) = 0, \quad (2.4)$$

$$\mathbf{v} \left(x + \frac{2\pi n}{\alpha}, y + \frac{2\pi m}{\beta}, z, t \right) = \mathbf{v}(x, y, z, t) \quad (n, m = 1, 2, \dots). \quad (2.5)$$

Equation (2.4) imposes the no-slip condition at the wall, whereas (2.5) are periodic boundary conditions in the streamwise and spanwise directions. While the choice of periodic rather than inflow–outflow boundary conditions in the streamwise direction may affect primary instability, it is expected that periodicity will not seriously modify the secondary instability discussed later because, as will be seen, the eigenfunction associated with secondary instability has excitation quite localized (within a given periodicity length) in the streamwise direction.

For plane Poiseuille flow (in which the dimensionless basic flow is given by $U_{\parallel} = 1 - z^2$, $(-1 \leq z \leq 1)$), linear instability occurs at $R_c = 5772$ (Orszag 1971). Squire's theorem implies that the critical disturbance is two-dimensional ($x - z$): the critical wavenumber is $\alpha_c = 1.02$. Since the instability in this flow is induced by viscosity, the growth rates are typically very small compared to the convective timescale (the latter being $O(1)$ in our non-dimensionalization of (2.2)).

For example, the most rapidly growing exponential instability of plane Poiseuille flow occurs at $R_{\text{opt}} \approx 48000$; the wavenumber of the disturbance is $\alpha = 0.79$ and its growth rate is $\operatorname{Im} \omega = 0.0076$. This optimal instability is so feeble that perturbations grow by a factor 10 in a time of about 300, in which time a point on the centreline moves about 150 channel widths. In contrast, transition is observed to occur explosively over a few channel widths at Reynolds numbers as low as roughly 1000.

Similar analyses of the linear stability of axisymmetric shear flows may be made in terms of cylindrical polar (x, r, θ) coordinates. In pipe Poiseuille flow, the undisturbed flow is $(1 - r^2) \hat{\mathbf{x}}$. To date, no linear instability (either axisymmetric or non-axisymmetric) has been found for the latter flow. Although there is no rigorous proof of the unconditional linear stability of pipe flow, we accept this result and seek the cause for transition in this flow elsewhere.

In the above description of linear stability theory, a modal decomposition of the perturbation flow field is assumed with individual modes behaving exponentially in time. However, in the absence of viscosity, there are disturbances of parallel shear flows that grow algebraically in time (Stuart 1965; Ellingsen & Palm 1975; Landahl 1980). Ellingsen & Palm show that disturbances that are independent of the streamwise direction have streamwise velocities that grow like t . At finite Reynolds numbers, the vortex-shearing mechanism responsible for this algebraic growth persists only for a finite time. However, before these disturbances decay at large times owing to diffusion and distortion by the mean flow, they can be amplified significantly. To investigate this phenomenon, we have considered the evolution of that disturbance that is energetically most favourable (i.e. that disturbance which is most effective in initially extracting energy from the mean flow) in plane Poiseuille flow at $R = 1000$. The form of this disturbance is known to be independent of the streamwise direction (Busse 1969). With $\alpha = 0$, $\beta = 1.5$, the disturbance reaches a maximum amplitude amplification of roughly 10 in a time of 70, after which it decays. Although this amplification is significant when compared to those predicted by linear modal analysis it is small relative to those of our three-dimensional secondary instability. We conclude that algebraic mechanisms most probably do not play a major role in 'noisy' experiments. However, in carefully controlled situations they may prove important in achieving the finite-amplitude secondary-flow states required to initiate secondary instability.

3. Nonlinear saturation of primary instability

To study nonlinear saturation of the primary two-dimensional instability in plane Poiseuille flow, the velocity is written

$$\mathbf{v}^{(2)} = U_{\parallel}(z) \hat{\mathbf{x}} + \sum_{n=-N}^N \mathbf{v}_n^{(2)}(z, t) e^{ianx}. \quad (3.1)$$

Reality requires

$$\mathbf{v}_n^{(2)} = \mathbf{v}_{-n}^{(2)\dagger} \quad (3.2)$$

(\dagger denoting complex conjugate). Equation (3.1) is the nonlinear extension of (2.1), and must therefore include (at least in principle) all Fourier modes in x , i.e. $N = \infty$. Note that the total mean (parallel) flow is no longer given by the basic flow U_{\parallel} ($= 1 - z^2$) in (3.1) but rather by $U'_{\parallel} = U_{\parallel} + u_0^{(2)}$. Therefore the flow is normalized not by its centreline velocity or mass flux but rather by the fixed mean pressure gradient, $2/R$.

It has been shown numerically that, for a wide class of perturbations and Reynolds numbers, the two-dimensional velocity field can be further specified as

$$\mathbf{v}^{(2)} = U_{\parallel}(z) \hat{\mathbf{x}} + \sum_{n=-N}^N \mathbf{v}_n^{(2)}(z, \tau) e^{ian(x-ct)}, \quad (3.3)$$

where two timescales are distinguished. The first timescale t is that for propagation of the nonlinear waves (3.3); here the real wavespeed is given by c . The second timescale τ is that for attenuation of the travelling waves, and is related to t by

$$\tau = tR^{-1}. \quad (3.4)$$

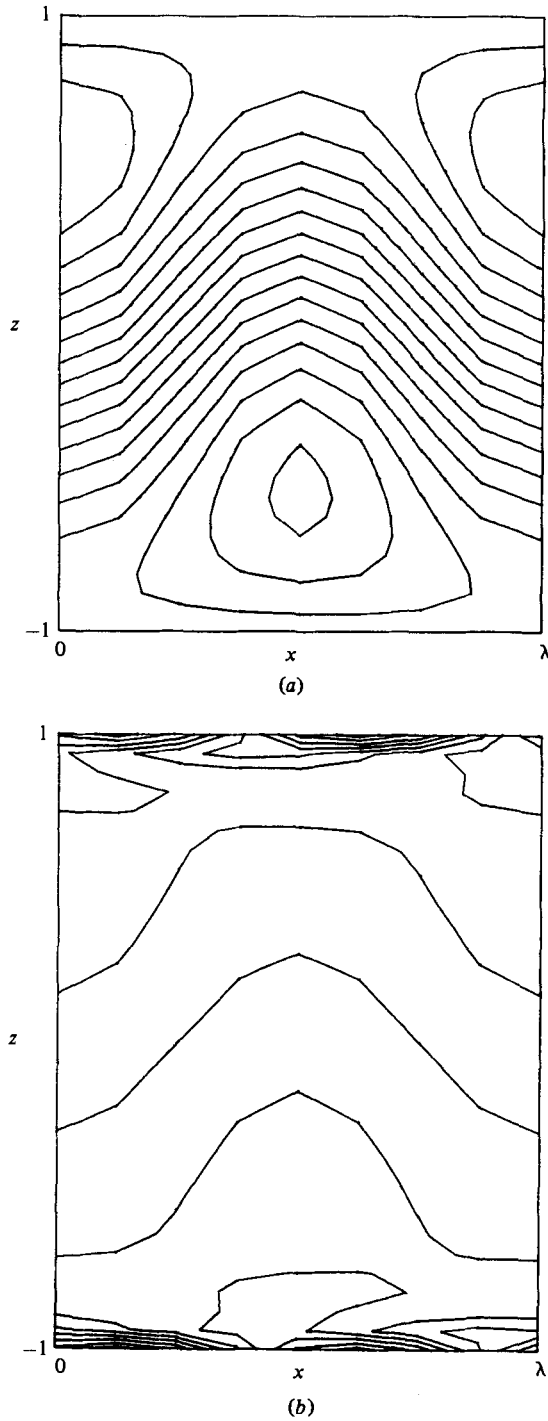


FIGURE 1. Stream (a) and vorticity (b) contours of the steady (stable) finite-amplitude two-dimensional plane Poiseuille flow (3.1) at $R = 4000$, $\alpha = 1.25$ plotted in a coordinate system moving with the wave speed c . Here $\lambda (= 2\pi/\alpha)$ is the wavelength of the primary disturbance. The finite-amplitude wave appears as counter-rotating eddies in this frame. Note that in the interior of the flow (where viscosity is unimportant) the vorticity contours are very similar to the streamlines. This implies that vorticity is nearly convected along streamlines away from the boundaries.

To classify the solutions (3.3) it is helpful to define the energy (normalized with respect to that of U_{\parallel}) in the n th streamwise Fourier mode by

$$E_n^{(2)} = \frac{15}{8(1 + \delta_{0n})} \int_{-1}^1 (\mathbf{v}_n^{(2)} \cdot \mathbf{v}_n^{(2)\dagger}) dz \quad (3.5)$$

and the total two-dimensional energy by

$$E^{(2)} = \sum_{n=1}^N E_n^{(2)}. \quad (3.6)$$

On the nonlinear neutral surface in $(E^{(2)}, R, \alpha)$ -space, exact solutions of the Navier-Stokes equations of the form (3.3) exist with no dependence on the time scale τ . Such equilibrium solutions are denoted (in the laboratory frame) by $\mathbf{v}_{\text{eq}}^{(2)}$. The salient features of this nonlinear neutral surface are as follows:

- (i) The slice $E^{(2)} = 0$ in the (R, α) -plane is the linear neutral surface;
- (ii) No finite-amplitude neutral (non-attenuated travelling wave) solutions exist below $R \approx 2900$ (Grohne 1969; Herbert 1976);
- (iii) For $R \gtrsim 2900$, neutral finite-amplitude solutions exist for a finite band of wavenumbers (centred about $\alpha \simeq 1.25$ of width $\Delta\alpha \approx 0.5$ for subcritical R) (Herbert 1976);
- (iv) For $R < 5772$, at any given α there are either zero or two finite-amplitude equilibria. If there are two, the lower-energy ('lower-branch') solution is unstable to two-dimensional perturbations, while the higher-energy ('upper-branch') solution is stable to all two-dimensional perturbations with x -period $2\pi/\alpha$.

The states on the nonlinear $(E^{(2)}, R, \alpha)$ -surface include both nonlinearly saturated linearly unstable modes (for $R > 5772$) as well as additional subcritical states (for $R \gtrsim 2900$) which arise from nonlinear primary instability.

The existence of the slow timescale τ in the evolution of general nonlinear two-dimensional disturbances can be inferred from the existence of equilibria which are independent of τ . To wit, we write the two-dimensional Navier-Stokes equations as

$$\frac{\partial \zeta}{\partial t} + J(\psi, \zeta) = \frac{1}{R} \nabla^2 \zeta, \quad (3.7)$$

where ψ is the stream function, $\zeta = \nabla^2 \psi$ is the y -vorticity and J is the Jacobian operator. In a frame of reference travelling with a two-dimensional equilibrium, (3.7) reduces to

$$J(\bar{\psi}, \bar{\zeta}) = \frac{1}{R} \nabla^2 \bar{\zeta}, \quad (3.8)$$

where $(\bar{\psi}, \bar{\zeta})$ is the equilibrium solution. In the interior of the flow the $R \rightarrow \infty$ limit is non-singular so that

$$\bar{\zeta} = g(\bar{\psi}) + O(1/R) \quad (3.9)$$

for some function g . The validity of (3.9) is demonstrated in figure 1, in which vorticity ($\bar{\zeta}$) contours and streamlines (contours of $\bar{\psi}$) are plotted; it is seen that $\bar{\zeta}$ and $\bar{\psi}$ do in fact have the same form in the interior of the flow.

To find the timescale of approach to the equilibrium, the steady-state solution is perturbed into

$$\psi = \bar{\psi} + \epsilon \psi', \quad \zeta = \bar{\zeta} + \epsilon \zeta' \quad (\epsilon \ll 1). \quad (3.10)$$

Inserting (3.10) into (3.7) and linearizing with respect to ϵ gives

$$\frac{\partial \zeta'}{\partial t} + J(\psi', \bar{\zeta}) + J(\bar{\psi}, \zeta') = \frac{1}{R} \nabla^2 \zeta'. \quad (3.11)$$

For perturbations of the special form

$$\psi' \propto \bar{\psi}, \quad \zeta' \propto \bar{\zeta} \quad (3.12)$$

the Jacobian terms in (3.11) vanish, so that disturbances of this type will decay only on a viscous timescale, dominating other modes as $t \rightarrow \infty$. It has been shown numerically (Orszag & Patera 1980, 1981*a*) that such *quasi-equilibria* evolving only on the long timescale in fact exist for deviations from $(\bar{\psi}, \bar{\zeta})$ much larger than those formally valid in deriving (3.11). Indeed, quasi-equilibria exist even for Reynolds numbers well below 2900 (although they must decay at large times at these low R). At $R = 1500$, $\alpha = 1.32$, the decay of a finite-amplitude perturbation is about four times slower than that of the corresponding linear mode. The fact that the slow timescale is relevant even below $R = 2900$ implies that plane Poiseuille flow has effectively stationary secondary states down to quite low Reynolds number.

The quasi-equilibria appear to be the dominant feature of the nonlinear two-dimensional states of plane Poiseuille flow. The long-time evolution of these flows (as determined by direct numerical solution of (2.2)–(2.5)) appears smooth and regular with no hint of the chaos of real, turbulent flows.

In contrast with plane Poiseuille flow, pipe flow is linearly stable, so axisymmetric equilibria can only exist if nonlinearity is destabilizing. Numerical solution of the Navier–Stokes equations show that initial states predicted to be nonlinearly dangerous by amplitude expansion methods (Davey & Nguyen 1971; Itoh 1977) are, in fact, stable and decay rapidly in t (Patera & Orszag 1981). It is tentatively concluded that pipe Poiseuille flow is stable to all finite-amplitude axisymmetric disturbances. Furthermore, our numerical solutions suggest that the slow timescale τ for evolution of two-dimensional states in plane Poiseuille flow does not hold in the evolution of axisymmetric perturbations of pipe flow.

4. Linear secondary instability

In this section, we study the stability of two-dimensional equilibria and quasi-equilibria of plane Poiseuille flow to infinitesimal three-dimensional perturbations. The analysis is also extended to the more complicated case of pipe Poiseuille flow where no quasi-equilibria or equilibria seem to exist.

The flows to be studied are assumed to be of the form of a general two-dimensional velocity on which an infinitesimal three-dimensional disturbance is superposed:

$$\mathbf{v} = U_{\parallel}(z) \hat{\mathbf{x}} + \sum_{n=-N}^N \mathbf{v}_n^{(2)}(z, t) e^{i\alpha n x} + \epsilon \mathbf{v}^{(3)} \quad (\epsilon \ll 1), \quad (4.1a)$$

$$\mathbf{v}^{(3)} = \sum_{m=\pm 1} \sum_{n=-N}^N \mathbf{v}_{nm}^{(3)}(z, t) e^{i\beta m y} e^{i\alpha n x}. \quad (4.1b)$$

Here $\mathbf{v}^{(k)}$ refers to the k -dimensional perturbation (infinitesimal when $k = 3$). Only one mode is kept in the y -direction (spanwise wavenumber β) owing to linearity and separability; N modes are kept in the streamwise direction owing to nonlinear effects. Continuing the multiple-timescale formalism introduced in §3, the general form of the velocity (4.1) is

$$\begin{aligned} \mathbf{v} = & U_{\parallel}(z) \hat{\mathbf{x}} + \sum_{n=-N}^N \mathbf{v}_n^{(2)}(z, \tau) e^{i\alpha n(x-ct)} \\ & + \epsilon \left\{ \sum_{m=\pm 1} e^{\sigma_m t} \sum_{n=-N}^N \mathbf{v}_{nm}^{(3)}(z, \tau) e^{i\beta m y} e^{i\alpha n(x-ct)} \right\} \quad (\epsilon \ll 1). \end{aligned} \quad (4.2)$$

Three kinds of analysis are now possible. First, we can do an exact linear (in ϵ) stability analysis for $R > 2900$. Here, two-dimensional equilibria exist which do not depend on the timescale τ . Making a Galilean transformation to the frame of reference travelling with speed c (phase speed of the equilibrium) the problem is separable in t , and (4.2) simplifies to

$$\begin{aligned} \mathbf{v} = & \{U_{||}(z) - c\} \hat{\mathbf{x}} + \sum_{n=-N}^N \mathbf{v}_n^{(2)}(z) e^{i\alpha n x'} \\ & + \epsilon \sum_{m=\pm 1} e^{\sigma_m t} \sum_{n=-N}^N \mathbf{v}_{nm}^{(3)}(z) e^{i\beta m y} e^{i\alpha n x'} \quad (\epsilon \ll 1), \end{aligned} \quad (4.3)$$

where $x' = x - ct$. Similar analyses of the three-dimensional stability of two-dimensional flow states have been given by Clever & Busse (1974) for Bénard convection and Pierrehumbert & Widnell (1982) for periodic arrays of inviscid vortices.

Secondly, an approximate linear stability analysis can be performed for $R < 2900$, the variation of $\mathbf{v}^{(2)}$ on the slow timescale τ being neglected. Such an analysis proceeds identically as the first (i.e. (4.3) is still assumed), but $\mathbf{v}^{(2)}$ is no longer an exact solution to the steady two-dimensional Navier–Stokes equations. (Clearly this analysis is only valid for R sufficiently large. More precisely, it is valid only if $\sigma\tau = O(\sigma R) \gg 1$, so predictions of neutral stability, $\sigma = 0$, are merely formal. Here $\sigma = \text{Re } \sigma_m$.)

Thirdly, a direct (time-dependent) numerical solution of the flow (4.1) can be obtained. To wit, the evolution of the flow developing from initial conditions consisting of a finite-amplitude two-dimensional disturbance and an infinitesimal three-dimensional perturbation is found by solving the three-dimensional Navier–Stokes equations. The instability is detected by following the energies of the two-dimensional and three-dimensional components in (4.1):

$$E^{(2)} = \sum_{n=1}^N \frac{15}{8} \int_{-1}^1 (\mathbf{v}_n^{(2)} \cdot \mathbf{v}_n^{(2)\dagger}) dz, \quad (4.4a)$$

$$E^{(3)} = \epsilon^2 \sum_{m=\pm 1} \sum_{n=0}^N \frac{15}{8(1+\delta_{0n})} \int_{-1}^1 (\mathbf{v}_{nm}^{(3)} \cdot \mathbf{v}_{nm}^{(3)\dagger}) dz = \epsilon^2 \sum_{n=0}^N E_n^{(3)}. \quad (4.4b)$$

The first two methods are semi-analytical in the sense that the time domain is handled analytically (e.g. as an eigenvalue problem). These methods are less general than the third (and cannot be readily extended to high resolution in x, z), but they are computationally fast at low resolution, eliminate transients, and can be used to determine the basic parametric dependence of the instability.

Let us now turn to the results of the linear stability eigenvalue calculations for plane Poiseuille flow. Upon inserting (4.3) into the incompressible Navier–Stokes equations and linearizing with respect to ϵ one obtains the stability equations (Orszag & Patera 1981 a).

$$\begin{aligned} & \left\{ \sigma_m (D^2 - k_{nm}^2) - \frac{1}{R} (D^2 - k_{nm}^2)^2 \right\} w_{nm} - im\beta D \{ (\bar{U} * v_x)_{nm} + (\bar{W} * v_z)_{nm} \} \\ & - i\alpha D \{ (\bar{U} * u_x)_{nm} + (u * \bar{U}_x)_{nm} + (\bar{W} * u_z)_{nm} + (w * \bar{U}_z)_{nm} \} \\ & - k_{nm}^2 \{ (\bar{U} * w_x)_{nm} + (u * \bar{W}_x)_{nm} + (\bar{W} * w_z)_{nm} + (w * \bar{W}_z)_{nm} \} = 0, \end{aligned} \quad (4.5)$$

$$\begin{aligned} & \left\{ \sigma_m - \frac{1}{R} (D^2 - k_{nm}^2) \right\} \zeta_{nm} - i\alpha n \{ (\bar{U} * v_x)_{nm} + (\bar{W} * v_z)_{nm} \} \\ & + im\beta \{ (\bar{U} * u_x)_{nm} + (u * \bar{U}_x)_{nm} + (\bar{W} * u_z)_{nm} + (w * \bar{U}_z)_{nm} \} = 0, \end{aligned} \quad (4.6)$$

$$i\alpha n u_{nm} + i\beta m v_{nm} + D w_{nm} = 0, \quad (4.7)$$

$$i\beta m u_{nm} - i\alpha n v_{nm} = \zeta_{nm}, \quad (4.8)$$

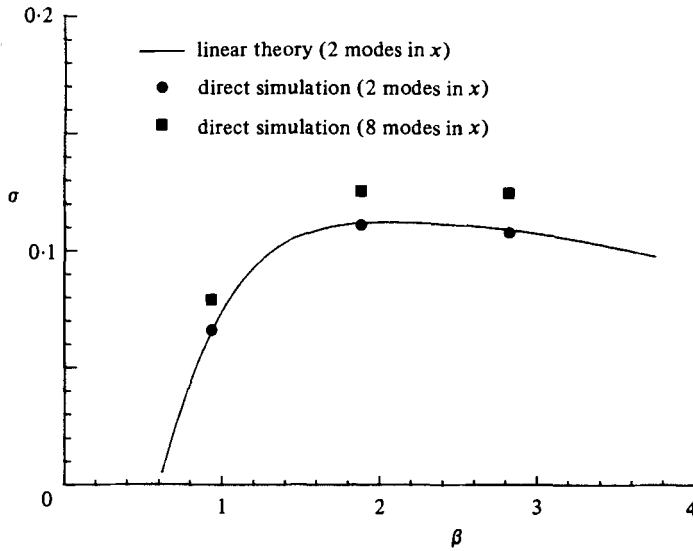


FIGURE 2. A plot of the growth rate σ of three-dimensional disturbances as a function of spanwise wavenumber β when $\alpha = 1.25$, $R = 4000$ in plane Poiseuille flow. Here the two-dimensional background state (assumed steady in the moving frame) is an equilibrium solution of the Navier-Stokes equations. The positive sign is taken for the symmetry (4.11). Note the large (convective) growth rates.

where D denotes d/dz , $k_{nm}^2 = \alpha^2 n^2 + \beta^2 m^2$, $()_x$ denotes d/dx_i and an asterisk $*$ indicates convolution:

$$(\bar{h} * g)_{nm} = \sum_{\substack{p+q=n \\ |p|, |q| \leq N}} \bar{h}_p g_{qm}. \tag{4.9}$$

Also, (\bar{U}, \bar{W}) is the two-dimensional (steady) flow $\mathbf{v}_{eq}^{(2)} - c\hat{x}$, and (u_{nm}, v_{nm}, w_{nm}) is the three-dimensional perturbation, $\mathbf{v}_{nm}^{(3)}$.

Equations (4.3)–(4.8) are consistent with the following symmetries of $\mathbf{v}_{nm}^{(3)}$:

$$\mathbf{v}_{nm}^{(3)} = \mathbf{v}_{-n-m}^{(3)\dagger}, \quad \sigma_m = \sigma_{-m}^\dagger \tag{4.10}$$

$$\{u_{nm}(z), v_{nm}(z), w_{nm}(z)\} = \pm (-1)^{n+1} \{u_{nm}(-z), v_{nm}(-z), -w_{nm}(-z)\}, \tag{4.11}$$

$$\{u_{nm}, v_{nm}, w_{nm}\} = \pm \{u_{n-m}, -v_{n-m}, w_{n-m}\}. \tag{4.12}$$

The symmetry (4.11) is a spatial symmetry in z ; both sign possibilities will be investigated. Equation (4.12) implies reflectional symmetry in y . Together with the reality condition (4.10), it implies that $\text{Im} \sigma_m = 0$, i.e. that the three-dimensional wave is phase-locked with the two-dimensional field. This is suggested by direct simulations and is verified by the solution of (4.3)–(4.8). The three symmetries (4.10)–(4.12) make the numerical eigenvalue calculation much more tractable – the requirement that they be physically relevant will be shown to be satisfied later. Some details of the numerical techniques used to solve the eigenvalue problem are given in appendix I.

First, we consider the case where $R > 2900$ and (4.3) and, hence, (4.5)–(4.8) are exact. In figure 2, σ is plotted as a function of β at $R = 4000$, $\alpha = 1.25$ assuming the positive sign in (4.11). Note that for β greater than some threshold value three-dimensional perturbations grow on a convective timescale ($\sigma = O(1)$). Although maximum growth occurs at $\beta = O(\alpha)$, the preference in β is very weak. Beyond the

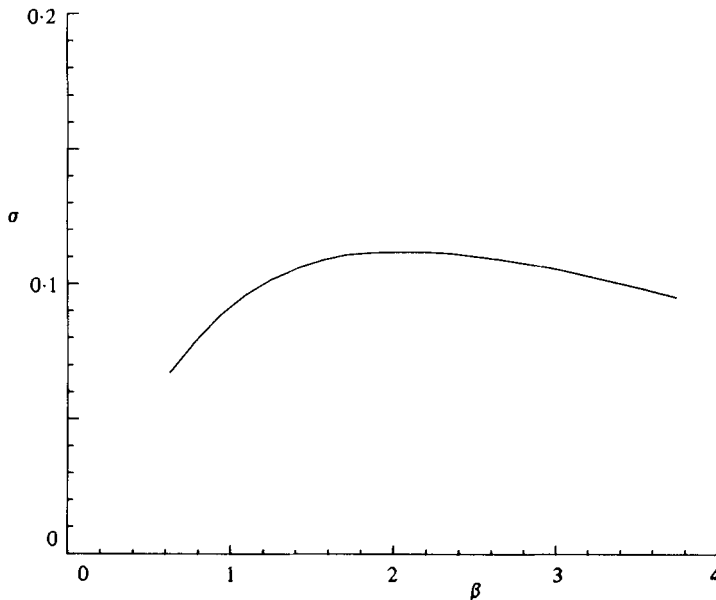


FIGURE 3. Same as figure 2, except that the negative sign is chosen for the symmetry (4.11).

threshold, the growth rate of the secondary instability is indeed quite large. With $\sigma = 0.15$, a disturbance grows in energy by a factor of 10 in a time of order 7, to be contrasted with the most dangerous linear Orr–Sommerfeld eigenmode that requires nearly two orders of magnitude larger time to achieve similar growth (even at $R_{\text{opt}} \approx 48000$).

The results of a direct numerical solution (using comparable resolution and starting with initial conditions with the positive symmetry (4.11)) are also plotted in figure 2. The good agreement with the linear theory is a useful test of both methods. (Some details of the numerical methods used here are given in appendix II.) The fact that the numerical solution conserves the symmetries (4.11), (4.12) but does not impose them implies that symmetry-breaking modes cannot be much more unstable than symmetry-preserving modes.

The effect of the symmetry (4.11) is investigated by repeating the stability calculation with the negative rather than the positive sign in (4.11). The results are plotted in figure 3. The only significant difference between the results plotted in figures 2 and 3 is the apparent absence of a spanwise wavenumber threshold in the latter. We conclude that the general behaviour of an asymmetric-in- z disturbance is similar to that of the symmetrized modes (4.11). In the following β is typically of order unity, so the two signs in (4.11) give basically the same result; the positive sign will be used unless stated explicitly to the contrary. On the other hand, the symmetry (4.12) is a statement about the basic dynamics of the instability; from the direct simulation results it appears that any instabilities that do not satisfy (4.12) are weak compared with those that do. The phase locking of the two-dimensional and three-dimensional modes, and the symmetry (4.12), do not seem peculiar to plane Poiseuille flow, as will be demonstrated later.

The Reynolds-number dependence of the three-dimensional growth rate σ is important. An exact analysis of (4.5)–(4.8) can only be performed down to $R = 2900$. However, the analysis can be extended in an approximate way using the second stability analysis method outlined above. A two-dimensional equilibrium which

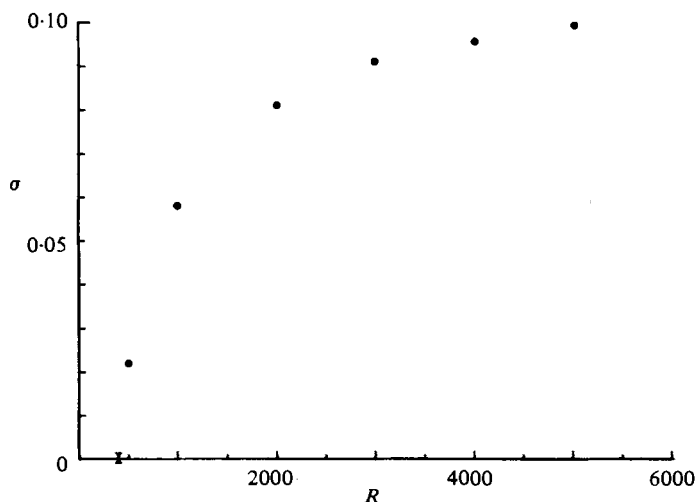


FIGURE 4. A plot of the growth rate σ of three-dimensional disturbances as a function of R when $\alpha = \beta = 1.25$. These results are obtained using the quasi-steady analysis explained in the text. Note the asymptotic independence of $\sigma(R)$ as $R \rightarrow \infty$.

actually obtains for $R > 2900$ (e.g. $R = 4000$) is chosen as the basic state in the stability analysis for $R < 2900$. As indicated previously, we are essentially neglecting here the slow timescale τ . The results of such a calculation for $\alpha = \beta = 1.25$ are given in figure 4 using the equilibrium computed at $R = 4000$, $\alpha = 1.25$. There are two points to be noted here. First, even in the absence of two-dimensional decay, three-dimensional growth turns off (for these particular parameter values) at $R \approx 400$. Thus this bounds the critical Reynolds number for the secondary instability, $400 \lesssim R < 2900$. Second, the instability is inviscid in the sense that as $R \rightarrow \infty$ the growth rate becomes independent of R . In particular, the elbow in the curve below which σ begins to become sensitive to R is at roughly $R = 1000$.

To verify the convergence (in N) of the results presented above and to calculate the three-dimensional stability characteristics exactly for low R requires a direct numerical calculation, i.e. the third method described above. In figure 5, we plot $\ln E^{(2)}$ and $\ln E^{(3)}$ versus time for various Reynolds numbers at $\alpha = \beta = 1.32$. The initial form of $\mathbf{v}^{(2)}$ is that of the least stable Orr-Sommerfeld linear mode at the chosen (R, α) . Its initial energy, as defined in (4.4), is chosen to be 0.04 (corresponding to a r.m.s. maximum perturbation streamwise velocity of about 20%). The initial form of $\mathbf{v}^{(3)}$ is chosen to be that of the least stable three-dimensional eigenfunction of the Orr-Sommerfeld equation. As predicted by the linear theory (4.5)–(4.8), there is strong exponential growth of the three-dimensional disturbance at high Reynolds number. Furthermore, as suggested by the quasi-steady analysis above, the Reynolds number at which viscous effects start to become important is roughly 1000. Indeed, the critical Reynolds number suggested by the results plotted in figure 5 is of order 1000. This number should be compared with the critical Reynolds number predicted by classical linear theory, $R_c = 5772$. The ‘critical’ Reynolds number 1000 cannot be taken as a precise number, for within the framework of linear secondary instability theory (where no higher three-dimensional modes are generated in y and $\mathbf{v}^{(3)}$ has no effect on $\mathbf{v}^{(2)}$) all infinitesimal *three*-dimensional disturbances decay as $t \rightarrow \infty$ for $R < 2900$ since all *two*-dimensional states ultimately decay.

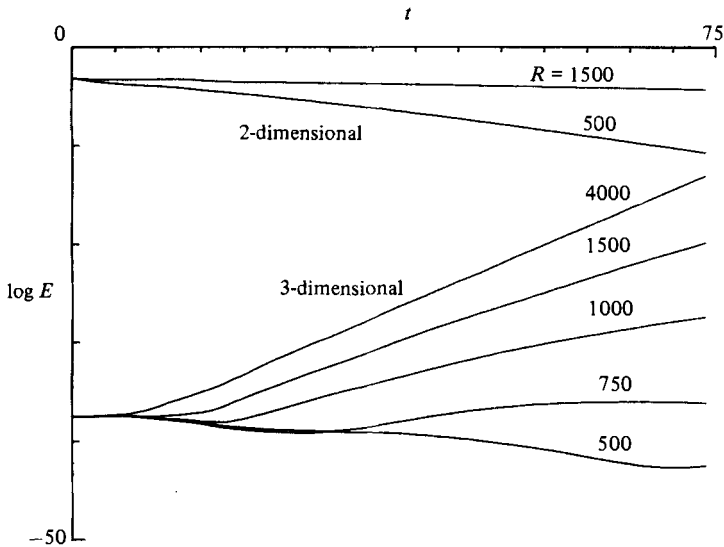


FIGURE 5. Reynolds-number dependence of the three-dimensional growth rate for plane Poiseuille flow at $\alpha = \beta = 1.25$. These results are obtained from a (time-dependent) direct numerical simulation. Observe that disturbances decay for $R < 1000$.

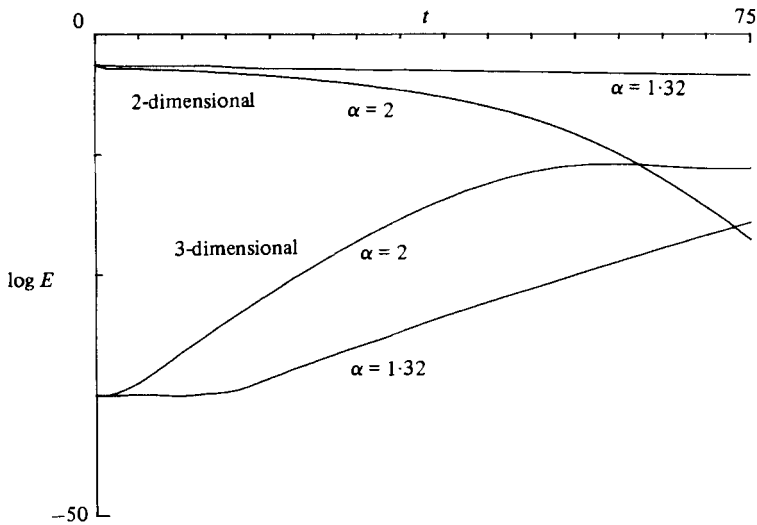


FIGURE 6. Streamwise wavenumber dependence of the three-dimensional growth rate in plane Poiseuille flow at $R = 1500$, $\beta = 1.32$.

To complete our somewhat cursory parametric mapping of linear secondary instability in plane Poiseuille flow we investigate the effect of streamwise wavenumber, α , and amplitude $A^{(2)}$ of $\mathbf{v}^{(2)}$. In figure 6 the results of a direct numerical simulation at a Reynolds number of 1500 are plotted for two different α . The results show that at $\alpha = 2.0$ three-dimensional growth is stronger than at $\alpha = 1.32$, but that two-dimensional decay at $\alpha = 2.0$ is significantly greater than at $\alpha = 1.32$. The fact that the results plotted in figure 4 give $R_c \gtrsim 400$ while those of figure 5 give $R_c = 1000$ implies that it is decay of the two-dimensional finite-amplitude disturbance that is

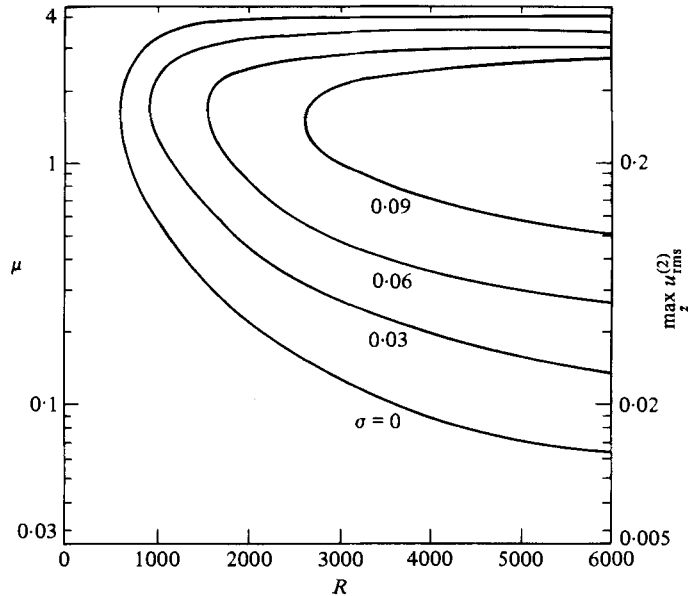


FIGURE 7. Contours of constant growth rate σ for three-dimensional perturbations of the primary two-dimensional state at $R = 4000$, $\alpha = 1.25$, rescaled by $\mu = A^{(2)}/A_{\text{eq}}^{(2)}$. The left-hand ordinate is μ , while the right-hand scale is the r.m.s. (in x, t) maximum (in z) streamwise perturbation velocity; the latter is roughly 17% when $\mu = 1$. Also, $E^{(2)} \approx 0.02$ when $\mu = 1$. Owing to contouring difficulties and limited numerical resolution, the contour shapes in this figure may be only qualitatively accurate.

primarily responsible for the viscous cutoff. It is for this reason that $\alpha = 1.32$ is chosen for the runs plotted in figure 5.

The effect of two-dimensional amplitude $A^{(2)}$ is most easily studied (at high Reynolds number) in the quasi-steady framework used above (see figure 4). The eigenvalue problem (4.5)–(4.8) is solved taking the actual equilibrium $\mathbf{v}_{\text{eq}}^{(2)}$ as the two-dimensional steady state with Fourier modes $\mathbf{v}_n^{(2)}$ for $n = 1, 2, \dots$ rescaled by $\mu = A^{(2)}/A_{\text{eq}}^{(2)}$, where $A_{\text{eq}}^{(2)}$ is the actual equilibrium amplitude. This analysis is justified for $\mu \approx 1$ by the existence of quasi-equilibria in a region of phase space around the equilibria. The results of this calculation are plotted in figure 7 in which curves of constant growth rate σ are plotted. Note the existence of a threshold amplitude at fixed R below which no three-dimensional perturbations grow, highlighting the requirement that the primary state be finite amplitude. The amplitude dependence of σ is fairly weak for $\mu \approx 1$, and the instability again turns off for large μ .

At this point we comment briefly on some experimental results due to Nishioka *et al.* (1975). In figure 15 of their paper, Nishioka *et al.* claim to distinguish a threshold amplitude for two-dimensional nonlinear instability. However, in figure 17 of the same paper they demonstrate spatial exponential growth rates of the nonlinear disturbance of the order of 0.3 (non-dimensionalized with respect to channel half-width), corresponding to a convective growth rate clearly indicative of three-dimensional, not two-dimensional, activity. Indeed, in a later paper, Nishioka *et al.* (1978) indicate that growth occurs virtually simultaneously with intense spanwise excitation. The reasonable agreement between some two-dimensional theories (e.g. Herbert 1977) and the three-dimensional results of Nishioka *et al.* is perhaps due to the fact that, at least for the parameters of figure 7 of the present paper, the strongest three-dimensional growth occurs for $\mu \approx 1$ and the threshold is not far below

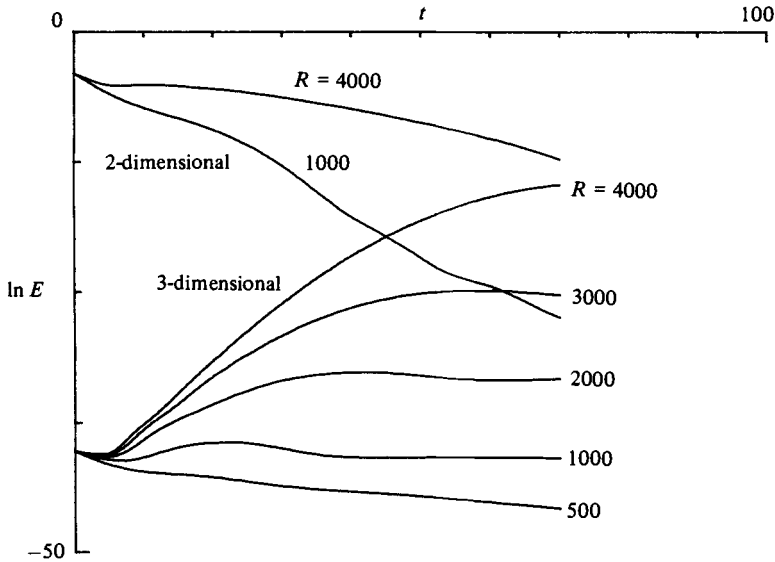


FIGURE 8. Reynolds-number dependence of the three-dimensional growth rate in pipe flow at $\alpha = 1.0$, $\beta = 1$. Results here are obtained using a direct numerical simulation. Note the very strong two-dimensional decay.

this. Note that the threshold for three-dimensional growth being at $\mu < 1$ is consistent with the disparity between theoretical two-dimensional amplitude predictions and the experimental results of Nishioka *et al.* (1975), the latter indicating 'two-dimensional' (but, in reality, three-dimensional) thresholds well below the former (Herbert 1977).

The instability described above for plane Poiseuille flow would seem to rely heavily on the existence of two dimensional equilibria and quasi-equilibria. In the case of pipe flow, no such states have yet been found, and it would appear that there is no hope of modelling transition by a secondary instability. However, although both the analysis and the results are less precise than in plane Poiseuille flow, secondary instability does in fact explain some aspects of pipe-flow transition.

Although the language of multiple-timescale analysis developed above will be used, the expansion (4.2) is no longer formally correct as there is no evidence of a slow timescale in pipe flow. Therefore, the only available procedure for determining pipe-flow stability is direct numerical solution of the time-dependent flow.

The equations for pipe Poiseuille flow will not be written in detail here. They are obtained from the equations for plane Poiseuille flow by the following replacements. The streamwise direction x becomes the axial direction, the spanwise direction y becomes the azimuthal direction θ , and the cross-stream direction z becomes the radial direction r . Velocities are denoted as before. The azimuthal wavenumber β is restricted to be integral. Two-dimensional modes now mean axisymmetric modes, while three-dimensional modes refer to non-axisymmetric modes. The extent to which pipe-flow simulations differ from planar-geometry simulations (in particular, the resolution of the pole problem) is discussed in appendix III.

The results of calculations of pipe flows with $\alpha = 1$, $\beta = 1$, analogous to the plane Poiseuille flow results plotted in figure 5, are given in figure 8. The initial velocity field is assumed to be of the form (4.1). The form of $\mathbf{v}^{(2)}$ at $t = 0$ is that of the least-stable wall mode; its energy (with respect to that of the mean flow) is 0.04. Several comments on the results plotted in figure 8 are in order. First, at high Reynolds numbers (e.g.

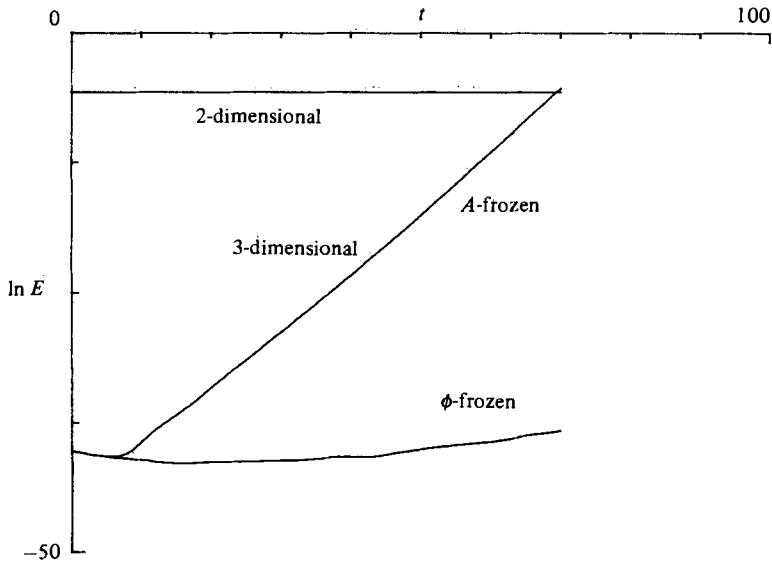


FIGURE 9. Effect of various two-dimensional forcing protocols on the three-dimensional growth rate in pipe flow. Freezing the phase of the two-dimensional flow results in no growth, whereas freezing the energy but allowing the phase relationships to develop naturally gives strong exponential growth.

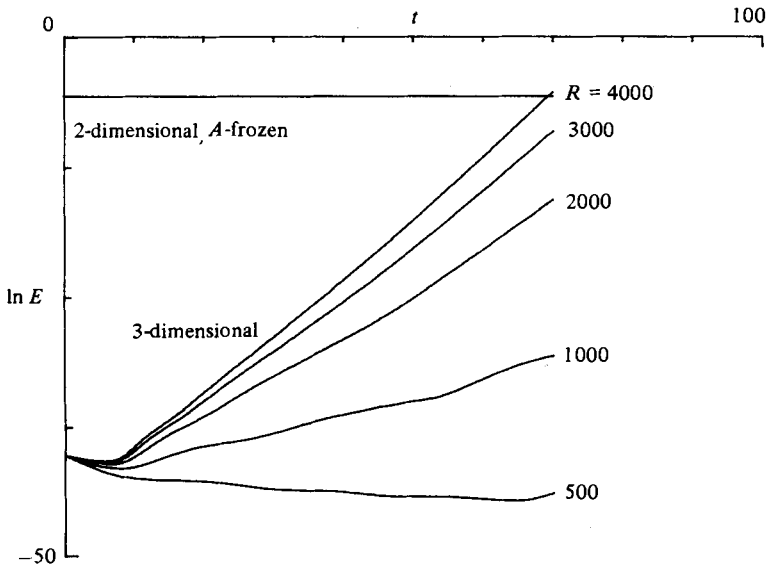


FIGURE 10. Reynolds-number dependence of the three-dimensional growth rate in pipe flow with an A -frozen two-dimensional field ($\alpha = 1.0$, $\beta = 1$).

4000) there is strong exponential growth of the three-dimensional perturbation for fairly long times. This should be contrasted with linear theory, which predicts stability at all Reynolds numbers. At a Reynolds number of 4000, a three-dimensional perturbation would have to be truly infinitesimal not to reach finite amplitudes before being cut off by the decay of the finite-amplitude two-dimensional disturbance. However, this growth requires large two-dimensional amplitudes whose origin (e.g.

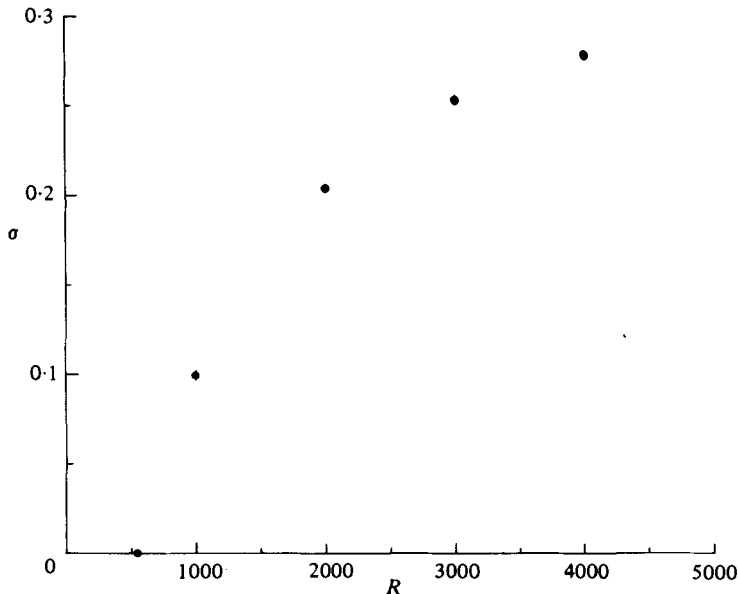


FIGURE 11. A plot of the three-dimensional growth rate in pipe flow as a function of Reynolds number ($\alpha = 1.0$, $\beta = 1$). Note the bend in the curve at $R = 1000$ – 3000 .

external noise, algebraic streamwise vortex growth) is not discussed here. Secondly, at Reynolds numbers of the order of 1000, two-dimensional decay is dominant; although three-dimensional disturbances are clearly damped at $R = 500$, it is difficult to distinguish a critical Reynolds number as clearly as for plane Poiseuille flow.

To determine a critical Reynolds number for secondary instability in pipe flow we resort to the artifice of forcing the axisymmetric part of the flow to have fixed amplitude. (Although this could conceivably be done within the framework of an eigenvalue problem, it is more easily done as a direct simulation.) There are two ways to force the flow and maintain the energy of the axisymmetric flow: the first, termed ϕ -frozen (phase-frozen), resets the axisymmetric field after each time step to its value at $t = 0$; the second, denoted A -frozen (amplitude frozen), normalizes the flow after each time step by the factor $(\bar{E}^{(2)}/\hat{E}^{(2)})^{1/2}$, where $\hat{E}^{(2)}$ is the energy of the axisymmetric flow before normalization, and $\bar{E}^{(2)}$ is the desired (constant) axisymmetric energy. If the two timescales t and τ did exist in this flow, ϕ -frozen would correspond to eliminating both the t - and τ -scales, whereas A -frozen would only eliminate the attenuation time τ . In particular, A -freezing does not prohibit nonlinear wave propagation, whereas ϕ -freezing does. At $R = 4000$, $\alpha = 1.0$, the evolution of a non-axisymmetric disturbance in both the ϕ -frozen and A -frozen cases is plotted in figure 9. In the former case there is no growth, whereas in the latter there is strong exponential growth. This illustrates the importance of the phase relationship between the two-dimensional and three-dimensional waves (as suggested by the symmetry (4.12)).

Next, the numerical experiment whose results are plotted in figure 8 is repeated with an A -frozen axisymmetric field. The results are plotted in figure 10. A critical Reynolds number is in fact implied by figure 10, but can be better seen by plotting the growth rates σ (obtained from figure 10) as a function of R . This is done in figure 11. It is seen that there is an elbow in the curve for $1000 < R < 3000$; below this elbow viscous effects are important, whereas above it inviscid growth is dominant.

In summary, pipe flow is susceptible to a strong non-axisymmetric secondary instability of decaying axisymmetric states. At high Reynolds numbers exponential growth persists for long times, but at low Reynolds numbers the instability is rapidly cut off by axisymmetric decay. Assuming a mechanism for sustenance of the axisymmetric flow, we obtain a critical Reynolds number of 1000–3000. The results given in figures 8–10 are for $\beta = 1$ and axisymmetric finite-amplitude flows that have (initially) the form of the most-unstable (linear) wall mode. Further numerical experimentation with centre modes and higher- β modes may yield new kinds of results.

5. Dynamics of linear secondary instability in plane Poiseuille flow

The secondary instability described above involves the explosive growth of infinitesimal three-dimensional perturbations superposed on a combined flow consisting of a mean flow and a (relatively) small (but finite-amplitude) two-dimensional disturbance. One question concerning the instability is the energetic role of the two-dimensional flow. In particular, in the absence of the two-dimensional finite-amplitude flow, the instability turns off. However, it is not obvious whether the two-dimensional flow acts only as a catalyst, allowing the mean flow to transfer energy to the three-dimensional flow (which it could not do in the absence of the two-dimensional primary flow), or if the two-dimensional primary flow directly supplies energy to the three-dimensional component. To answer this question, we consider the energetics of the three-component system consisting of the mean flow, the two-dimensional component, and the three-dimensional modes. In terms of our previous decomposition into two-dimensional and three-dimensional components (see (4.1)), the new decomposition is

$$\mathbf{v}^{[1]} = (U_{\parallel}(z) + u_0^{(2)}(z)) \hat{\mathbf{x}}, \quad (5.1)$$

$$\mathbf{v}^{[2]} = \mathbf{v}^{(2)} - u_0^{(2)} \hat{\mathbf{x}}, \quad (5.2)$$

$$\mathbf{v}^{[3]} = \mathbf{v}^{(3)}. \quad (5.3)$$

The energetics of this system can then be written as

$$\frac{dE^{[1]}}{dt} = -T^{12} - T^{13} + D^{[1]}, \quad (5.4)$$

$$\frac{dE^{[2]}}{dt} = T^{12} - T^{23} + D^{[2]}, \quad (5.5)$$

$$\frac{dE^{[3]}}{dt} = T^{13} + T^{23} + D^{[3]}, \quad (5.6)$$

where $E^{[i]}$ is the energy in the i th component, T^{ij} is the transfer from the i th to the j th component, and $D^{[i]}$ is the (negative) dissipation in the i th component. (These terms are given explicitly in appendix IV.)

In figure 12, the terms in (5.6) (normalized by $E^{[3]}$) are plotted for $R = 4000$, $\alpha = \beta = 1.25$. It is apparent that T^{23} is much smaller than T^{13} ; in fact, T^{23} barely balances the dissipation term $D^{[3]}$. Although the results plotted in figure 12 confirm that the two-dimensional component acts like a catalyst (though this term may be inappropriate as will be discussed below), there is yet a further distinction to be made. Either $\mathbf{v}^{[2]}$ alters the mean flow so that it can give energy to $\mathbf{v}^{[3]}$, or $\mathbf{v}^{[2]}$ is required to mediate energy transfer to $\mathbf{v}^{[3]}$ from the mean flow that would not normally allow

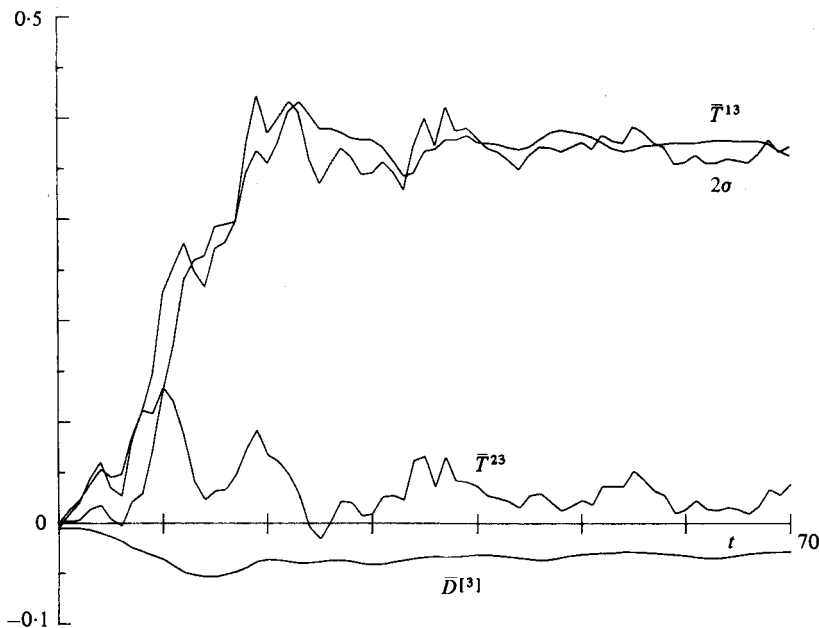


FIGURE 12. Energetics of secondary instability in plane Poiseuille flow. Note the transfer T^{13} between the mean flow and the three-dimensional disturbance is much larger than the transfer T^{23} from the two-dimensional primary to the three-dimensional secondary. The jagged nature of the curves is due to numerical noise in the direct simulation.

such persistent transfer. It may be shown that the latter is the case by repeating the run used to construct figure 12 but now freezing the mean flow to be the basic parabolic profile, i.e. $\mathbf{v}^{[1]} = U_{\parallel} \hat{\mathbf{x}}$ for all time (which we know is stable to infinitesimal disturbances at $R = 4000$). The results of this experiment are plotted in figure 13, where it is seen that the instability still obtains and T^{13} is still significantly greater than T^{23} . We remark that the 'catalyst' term is perhaps a misnomer, for T^{23}/T^{13} is in fact of order $(E^{[2]}/E^{[1]})^{1/2}$, the scaling that one would naturally expect from the definitions of the T^{ij} .

Although the above arguments indicate that the two-dimensional flow acts as a catalyst, they do not indicate how it catalyzes the instability. Two of the simplest classical arguments are as follows:

- (i) the two-dimensional flow creates locally (in x) inflexional streamwise profiles that are then susceptible to an inflexional instability;
- (ii) the two-dimensional flow creates curved streamline flow that is then unstable to Görtler rolls (Görtler & Witting 1958).

Neither of these highly simplified explanations can hope to explain all the features of the secondary instability presented in this paper; however, they do provide some useful insights. For instance, inflexion point (maximum-vorticity) arguments imply that the three-dimensional and two-dimensional waves should in fact travel at the same speed (see (4.12)). This follows by noting that, in analogy with the inviscid linear case, an unstable three-dimensional wave should travel with the velocity of $\mathbf{v}^{(2)}$ at that point where the vorticity ζ has a maximum. However, from (3.9) the vorticity maximum occurs roughly where ψ has a maximum, and hence in the steady frame it is stationary. Thus the three-dimensional disturbance must be steady in the steady frame of the two-dimensional wave, i.e. (4.12) holds

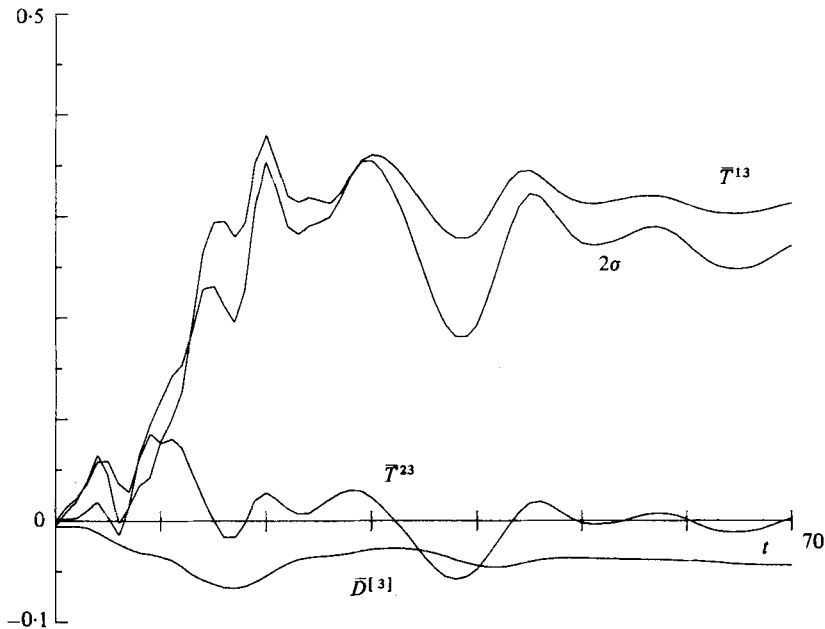


FIGURE 13. Energetics of secondary instability in plane Poiseuille flow with the mean flow frozen to be parabolic. Note T^{13} is still much larger than T^{23} , although T^{13} would in fact be negative if $E^{(2)}$ were sufficiently small.

Maximum-vorticity considerations can provide further insights. First, they predict that the three-dimensional disturbance eigenfunction should be localized near the two-dimensional whorl (point of maximum vorticity), which is indeed the case. Secondly, they provide a heuristic motivation for the amplitude dependence plotted in figure 7. It is easy to show that for small μ ($\mu = A^{(2)}/A_{\text{eq}}^{(2)}$) the point z_m at which ψ is maximized is near the wall, and moves out with increasing μ . For μ sufficiently large z_m leaves the viscosity-dominated wall region, so the inviscid instability mechanism can become operative. Once the inflexion point is clearly established, the instability is relatively insensitive to further modifications of $\mathbf{v}^{(2)}$. These arguments imply that the amplitude dependence (see figure 7) and other major features of the three-dimensional instability should hold in any wall-bounded flow with a sufficiently large two-dimensional perturbation, a hypothesis which is tested in §6. Despite these successes, inflexion-point considerations incorrectly predict the basic feature of the instability, namely its dimensionality. For, locally inflexional profiles should imply instability to two-dimensional disturbances (narrowly excited in x compared to the basic flow) as well as three-dimensional disturbances, whereas in fact only three-dimensional instability is obtained.

Explanation (ii) appears plausible, but it fails on several counts, as first noted in the observations of Klebanoff *et al.* (1962). First, it should be recognized that the instability outlined in §4 is significantly different from Görtler instability in that it must have streamwise dependence to exist. In fact, as shown below, the secondary instability is quite localized in x . Furthermore, the region of excitation of the three-dimensional perturbation eigenfunction is near the 'convex wall', not the 'concave' one as would be expected if the instability were driven by centrifugal force (see the end of this section).

The mechanism of secondary instability, in particular its three-dimensionality, is

perhaps best explained in terms of general vorticity dynamics. The analysis that follows is in fact a general description of some conditions on a flow such that it can be subject to an inviscid exponential instability.

To begin, the flow is decomposed as before into

$$\mathbf{v} = \mathbf{v}^{(2)} + \epsilon \mathbf{v}^{(3)}, \quad \boldsymbol{\omega} = \boldsymbol{\omega}^{(2)} + \epsilon \boldsymbol{\omega}^{(3)} \quad (\epsilon \ll 1), \quad (5.7), (5.8)$$

where $\boldsymbol{\omega} = \nabla \times \mathbf{v}$, $\mathbf{v}^{(2)}$ is defined in (3.1), and $\mathbf{v}^{(3)}$ is as given in (4.1). The linearized inviscid vorticity equation (neglecting viscous effects on the basis of the results plotted in figure 4) for the three-dimensional perturbation is then given by

$$\frac{\partial \boldsymbol{\omega}^{(3)}}{\partial t} = [(\boldsymbol{\omega}^{(3)} \cdot \nabla) \mathbf{v}^{(2)} - (\mathbf{v}^{(2)} \cdot \nabla) \boldsymbol{\omega}^{(3)}] + [(\boldsymbol{\omega}^{(2)} \cdot \nabla) \mathbf{v}^{(3)} - (\mathbf{v}^{(3)} \cdot \nabla) \boldsymbol{\omega}^{(2)}]. \quad (5.9)$$

There are two distinct effects represented in (5.9). The first bracketed term on the right-hand side will be called the stretching term; it mainly contributes owing to stretching of the x, z perturbation vorticity by the two-dimensional flow $\mathbf{v}^{(2)}$. The second bracketed term will be called the tilting term, its primary role being to tilt two-dimensional vorticity (which is solely in the y -direction) into the (x, z) -plane.

It may be shown that neither stretching nor tilting alone is sufficient to give exponential growth. With tilting alone, it follows that

$$\frac{\partial (\nabla \times \mathbf{v}^{(3)})}{\partial t} = \nabla \times (\mathbf{v}^{(3)} \times \boldsymbol{\omega}^{(2)}), \quad (5.10)$$

so that

$$\frac{\partial \mathbf{v}^{(3)}}{\partial t} = \mathbf{v}^{(3)} \times \boldsymbol{\omega}^{(2)} + \nabla \phi, \quad (5.11)$$

where ϕ is an arbitrary potential. Forming the energy gives

$$\frac{1}{2} \frac{d}{dt} \int (\mathbf{v}^{(3)} \cdot \mathbf{v}^{(3)}) d\mathbf{x} = \int \mathbf{v}^{(3)} \cdot (\mathbf{v}^{(3)} \times \boldsymbol{\omega}^{(2)}) d\mathbf{x} - \int (\mathbf{v}^{(3)} \cdot \nabla \phi) d\mathbf{x}. \quad (5.12)$$

The first term on the right-hand side vanishes, while the second can be converted into a surface integral (from incompressibility), which then vanishes owing to the boundary conditions. Thus tilting alone conserves energy and cannot give growth.

With stretching alone it follows that

$$\frac{\partial \boldsymbol{\omega}^{(3)}}{\partial t} = (\boldsymbol{\omega}^{(3)} \cdot \nabla) \mathbf{v}^{(2)} - (\mathbf{v}^{(2)} \cdot \nabla) \boldsymbol{\omega}^{(3)} = \nabla \times (\mathbf{v}^{(2)} \times \boldsymbol{\omega}^{(3)}), \quad (5.13)$$

so that

$$\frac{d}{dt} \int (\boldsymbol{\omega}^{(3)} \cdot \hat{\mathbf{y}})^2 d\mathbf{x} = 0.$$

As the eigenfunction grows exponentially everywhere in space, it follows that $\boldsymbol{\omega}^{(3)} \cdot \hat{\mathbf{y}} = 0$. Therefore the vorticity can be expressed as

$$\boldsymbol{\omega}^{(3)} = \nabla \times \psi \hat{\mathbf{y}}, \quad (5.14)$$

since $\nabla \cdot \boldsymbol{\omega}^{(3)} = 0$. Equation (5.13) then gives

$$\frac{\partial \psi}{\partial t} + (\mathbf{v}^{(2)} \cdot \nabla) \psi = - \frac{\partial \phi(y, t)}{\partial t}, \quad (5.15)$$

where ϕ is an arbitrary function. Including ϕ in the convective derivative (as $\mathbf{v}^{(2)} \cdot \hat{\mathbf{y}} = 0$) gives

$$\frac{\partial (\psi + \phi)}{\partial t} + (\mathbf{v}^{(2)} \cdot \nabla) (\psi + \phi) = 0, \quad (5.16)$$

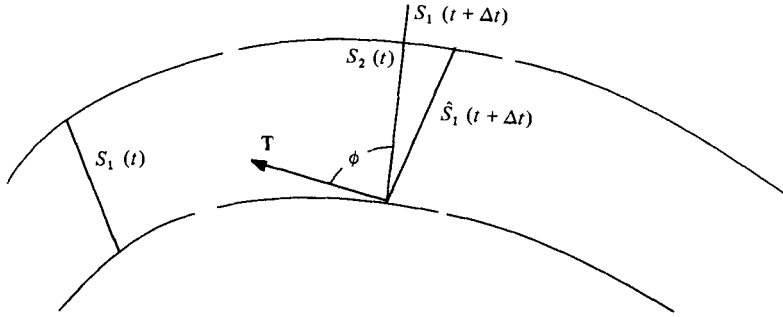


FIGURE 14. Simple tilting and stretching model for secondary instability. The vortex filament $S_1(t)$ is stretched into $\hat{S}_1(t + \Delta t)$ (the secondary flow $v^{(2)}$ is denoted by the dashed whorl) and then realigned by the tilting term to line up with $S_2(t)$ (but of larger magnitude than $S_2(t)$).

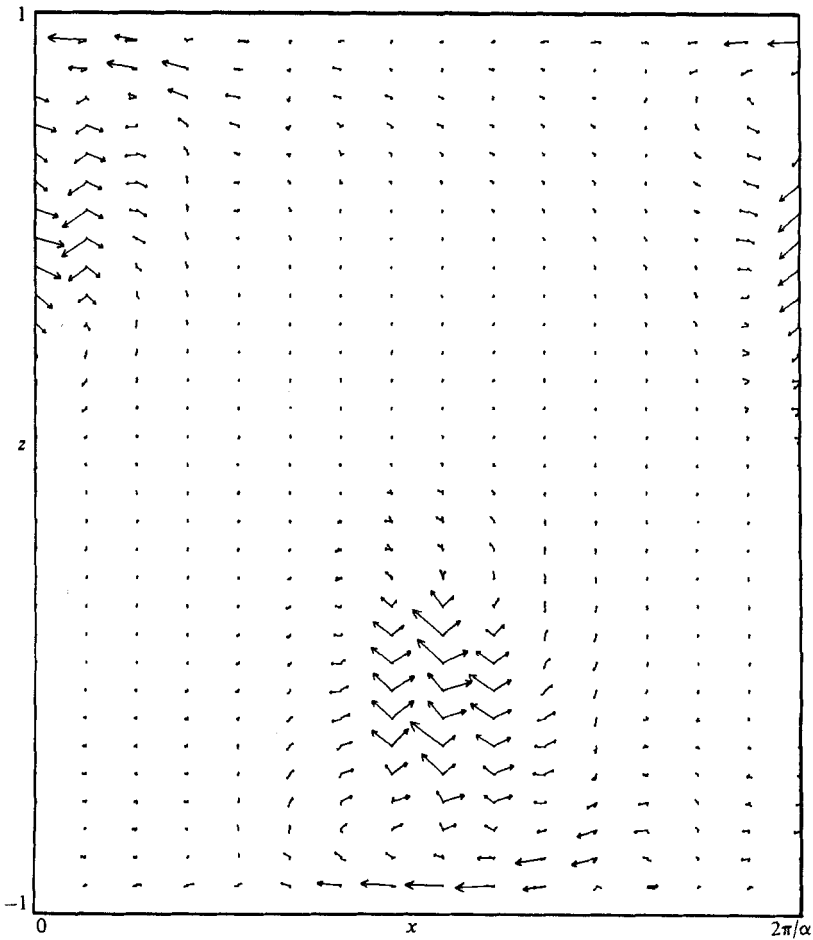


FIGURE 15. Tilting and x - z perturbation vorticity fields in plane Poiseuille flow at $R = 4000$, $\alpha = \beta = 1.25$. The vorticity field F is the clockwise rotating whorl near $z = -1$, $x = \pi/\alpha$; the tilting field T is nearly orthogonal to F where F is large.

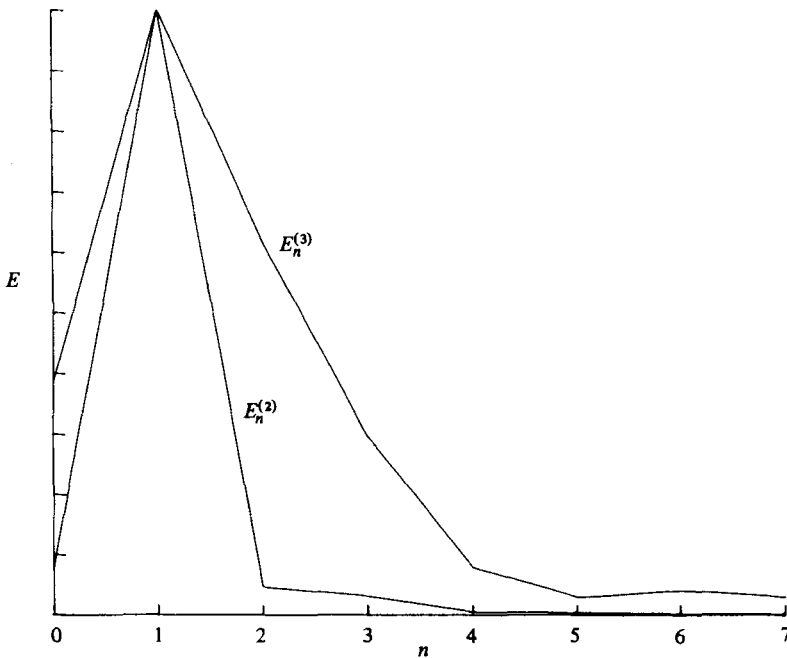


FIGURE 16. Streamwise-wavenumber spectra of $\mathbf{v}^{(2)}$ and $\mathbf{v}^{(3)}$ in plane Poiseuille flow. The spectra indicate that $\mathbf{v}^{(3)}$ is much more localized in x (within a given periodicity length) than $\mathbf{v}^{(2)}$.

from which it follows that no exponential modal growth can occur driven only by stretching. (Actually (5.16) implies that $\mathbf{v}^{(3)}$ must be a potential flow; the domain must be restricted (e.g. by requiring periodicity) to be such that no non-trivial potential flow exists.)

In a shear flow, one can easily obtain algebraic stretching of vortex lines (Ellingsen & Palm 1975); to obtain exponential growth we have shown above that both stretching and tilting are necessary. A simple scenario that explains the two roles is as follows. If only stretching were present, vortex lines would align with the shearing flow and algebraic growth would result. However, if tilting produces new vorticity (in the (x, z) -plane) that re-orientes the perturbation vorticity so as to prevent it from aligning with the streaming flow, exponential growth is possible. Therefore the actual stretching of the filaments is associated with the stretching term, while the redirection of the filaments is associated with the tilting term. A geometric picture of the process is given in figure 14; it is seen that the tilted primary vorticity is expected to be roughly orthogonal to the filaments of perturbation vorticity.

Let us define the filament and tilting vector fields as

$$\mathbf{F} = \boldsymbol{\omega}^{(3)} - (\boldsymbol{\omega}^{(3)} \cdot \hat{\mathbf{y}}) \hat{\mathbf{y}}, \tag{5.17}$$

$$\mathbf{T} = |\boldsymbol{\omega}^{(2)}| \beta(\mathbf{v}^{(3)} - (\mathbf{v}^{(3)} \cdot \hat{\mathbf{y}}) \hat{\mathbf{y}}) \tag{5.18}$$

respectively. (Here \mathbf{T} is the projection of the tilting term $\boldsymbol{\omega}^{(2)} \cdot \nabla \mathbf{v}^{(3)}$ in (5.9) into the (x, z) -plane, while \mathbf{F} is the projection of the perturbation vorticity field onto the (x, z) -plane.) Note that, since there is only one mode present in $\mathbf{v}^{(3)}$, the directions of both \mathbf{F} and \mathbf{T} are independent of y (modulo sign). The two fields are plotted in figure 15, where it is seen that, in fact, the two are nearly orthogonal.

There are several additional noteworthy features in figure 15. First, the three-

dimensional perturbation eigenfunction is highly localized in x (within a periodicity length), in contrast with the two-dimensional flow (which is the rationale behind ignoring the convective piece of the tilting term in the definition of \mathbf{T}). This can be seen as well in figure 16, in which a plot of the streamwise spectra of $\mathbf{v}^{(2)}$ and $\mathbf{v}^{(3)}$ is given. The half-width of the streamwise wavenumber spectrum of the three-dimensional disturbance is more than twice that of the two-dimensional one, implying that the region of excitation in physical space of the three-dimensional component is less than half that of the two-dimensional flow. With respect to possible Görtler instability, the region of excitation of $\mathbf{v}^{(3)}$ shown in figure 14 is around the whorl of $\mathbf{v}^{(2)}$; however, near the whorl, angular momentum is increasing outwards, and therefore one would not expect centrifugal instability.

6. Universality of secondary instability

The general nature of the arguments given above suggest that linear secondary instability should obtain in many shear flows. In this section, the analysis developed previously is applied to two additional flows, namely Blasius flow and plane Couette flow. As will be seen, secondary instability in Blasius flow and plane Couette flow is very similar to that in plane Poiseuille flow and pipe flow respectively, a fact that supports the idea that the instability studied here is common in shear flows.

Blasius flat-plate (zero-pressure-gradient) flow is not a parallel flow, the boundary-layer thickness growing with downstream distance x_0 like $(\nu x_0/U_0)^{1/2}$, where U_0 is the free-stream velocity. However, assuming parallel flow and setting the cross-stream velocity to zero, it is found that the linear stability characteristics of Blasius flow are very similar to those of plane Poiseuille flow. It is inviscidly stable, but viscosity is destabilizing for $R < R_c \approx 301$ (based on the lengthscale $\delta = (\nu x_0/U_0)^{1/2}$). The corresponding critical wavenumber is $\alpha_c = 0.179$.

The concept of periodic equilibria is ambiguous in a flow that evolves downstream. There are several formal ways to remedy this situation: the mean field can be completely frozen, or the mean field can evolve non-diffusively. The latter is more attractive in that it is then possible to see the effect of nonlinear interaction on the mean flow. In our simulations both diffusion and nonlinear interaction are allowed; for several reasons this does not affect the results in any significant way. First, the maximum time of integration is $0.25R$, all secondary instability results being established well before this point. Secondly, the transfer terms $T^{12} + T^{13}$ are typically 10 times bigger than the dissipation term $D^{[1]}$. For some details of the numerical simulation see appendix V.

The parameters for the direct simulation presented here are $R = 1000$, $\alpha = \beta = 0.50$. Initial conditions are of the form given in (4.1). As in the case of plane Poiseuille flow, two-dimensional quasi-equilibria (or equilibria – the distinction is somewhat blurred if one allows mean-flow diffusion) quickly form. For boundary layers the picture corresponding to figure 1 is given in figure 17; again note the coincidence of streamlines and vorticity contours in the interior of the flow. Note it appears that there are two-dimensional equilibria (with the mean flow restricted as above) at this α where linear theory predicts stability. It is also probable that there are subcritical equilibria.

As in the case of plane Poiseuille flow, the two-dimensional equilibria are exponentially unstable to infinitesimal three-dimensional disturbances, as shown in figure 18, in which a plot of $\ln E^{(2)}$ and $\ln E^{(3)}$ versus time is given. The growth rates are smaller (no doubt owing to the smaller α and lower Reynolds number). Again

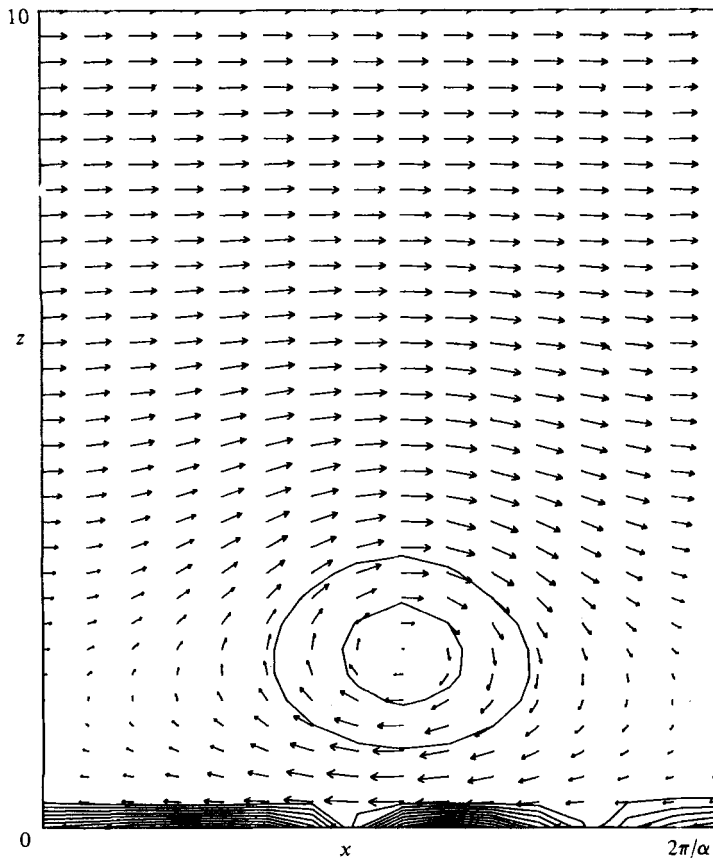


FIGURE 17. Two-dimensional quasi-equilibria in Blasius boundary-layer flow at $R = 1000$, $\alpha = 0.5$. Note the coincidence of vorticity contours and the streamlines (arrows) away from the walls.

T^{13} is roughly 10 times as large as T^{23} , and the x -spectrum of $\mathbf{v}^{(3)}$ is much broader than that of $\mathbf{v}^{(2)}$. The symmetry (4.12) holds (although (4.11) cannot), indicating that (as in the channel flow) the two- and three-dimensional waves move with the same phase speed (in this case $c \approx 0.5$). (The reason that the phase speed of the nonlinear Tollmien-Schlichting wave differs significantly from its linear counterpart in a boundary layer but not in plane Poiseuille flow is not yet understood.) Thus secondary instability in Blasius flow is quite similar to that in plane Poiseuille flow, although the parameter values at which it occurs are slightly different.

While it would certainly be more relevant to study the stability of quasi-equilibria in a growing boundary layer, the localized and strong instability found with the parallel-flow assumption and periodic boundary conditions is most likely a reasonable first approximation. Indeed, there seems no qualitative difference between the present results or those of Wray & Hussaini (1980) for full three-dimensional simulations of boundary-layer transition with periodic downstream boundary conditions and results obtained with inflow-outflow boundary conditions (Orszag 1976).

Plane Couette flow would superficially appear to be similar to plane Poiseuille flow. It is flow between parallel plates at $z = 1$, driven by motion of the walls, not a pressure gradient, with the basic laminar flow given by $\mathbf{U}_{||} = z\mathbf{x}$, $-1 \leq z \leq 1$. However, plane

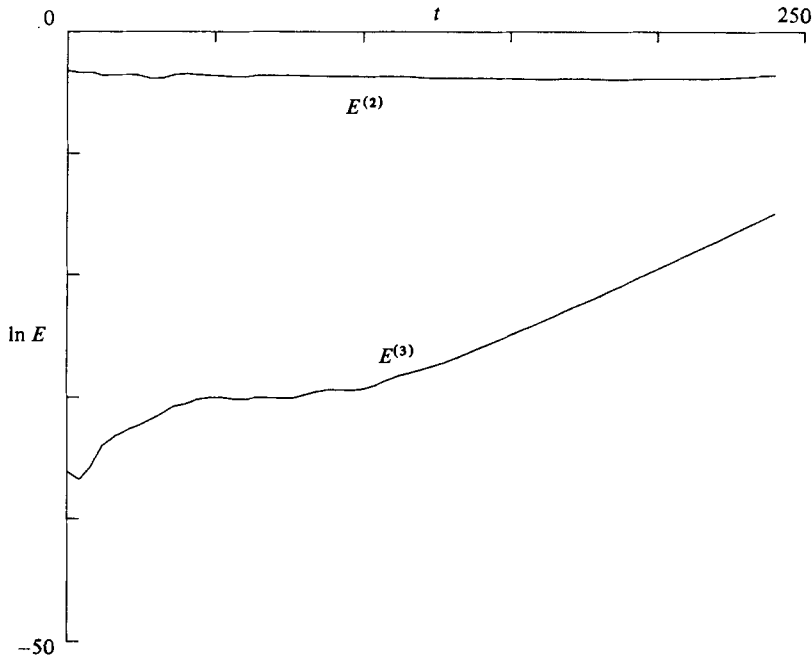


FIGURE 18. Three-dimensional secondary instability in boundary-layer flow. At $R = 1000$, $\alpha = \beta = 0.50$ three-dimensional disturbances grow exponentially with growth rates $\sigma \approx 0.04$.

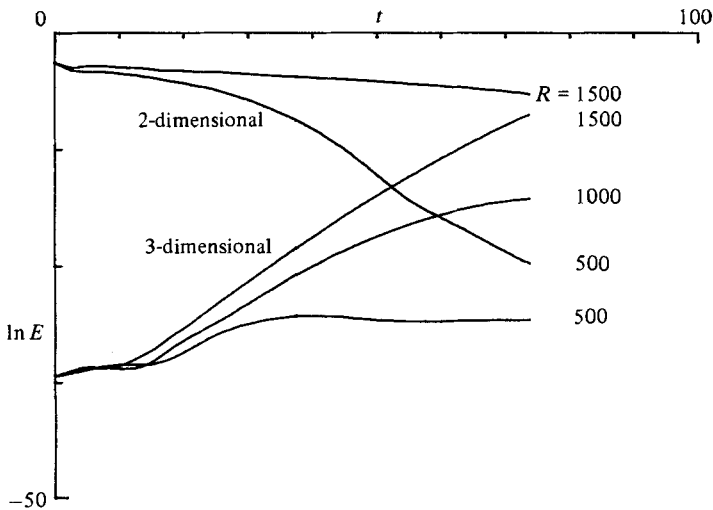


FIGURE 19. Three-dimensional secondary instability in plane Couette flow at $\alpha = \beta = 1.0$. A critical Reynolds number of 1000 is singled out.

Couette flow is in fact much more akin to pipe Poiseuille flow. First, although not proved rigorously, it appears that plane Couette flow is stable to all linear disturbances at all R (Davey 1973). Secondly, like pipe flow, there do not seem to be any finite-amplitude two-dimensional equilibria (Orszag & Patera 1981*b*), although their existence is predicted by low-order finite-amplitude expansions (Davey & Nguyen 1971; Ellingsen, Gjevik & Palm 1970).

As in the case of pipe flow, decaying secondary flows in plane Couette flow are

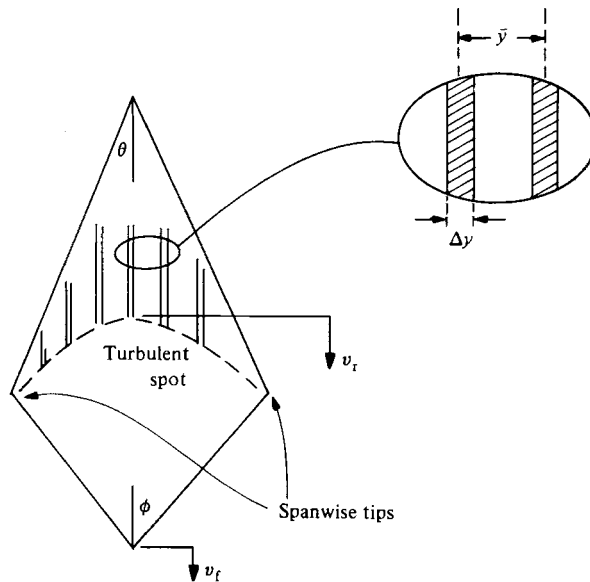


FIGURE 20. Schematic picture of turbulent spots observed in plane Poiseuille flow experiments (Carlson *et al.* 1981) at $R = 1000$. The features of interest are the spreading angle θ , the advancing angle ϕ , the streak spacing \bar{y} and the streak width Δy .

explosively unstable to infinitesimal three-dimensional perturbations. The results of a direct simulation of a plane Couette flow of the form (4.1) are given in figure 19 at $\alpha = \beta = 1.0$. Perturbations grow exponentially with growth rates comparable to those in plane Poiseuille flow. There is growth at $R = 1500$ but not at $R = 500$, implying a critical Reynolds number somewhere between these two limits. Although nonlinear two-dimensional decay is definitely much more pronounced than in plane Poiseuille flow, it is less than in pipe flow at low R . For this reason a critical Reynolds number can be ascertained without resorting to forcing the two-dimensional flow.

7. Secondary instability and transition

In determining the extent to which the secondary instability presented here relates to the physically occurring transition process, we can ask three questions:

- (i) does the basic parametric dependence predicted by the model agree with experiment;
- (ii) does the structure of the instability agree with that of early transition spots seen in experiments;
- (iii) does the instability lead to randomness and 'turbulence'?

In essence, these three questions address the role of secondary instability in early transition, late transition and turbulent flow respectively. The first question could be answered in detail with the tools we have developed; however, that is not our concern here. Furthermore, the reader should be warned that our discussions of the last two issues are extrapolative and exploratory in nature. In particular, in addressing question (ii), our use of a nonlinear periodic instability to explain a local phenomenon is meant only to indicate that a common mechanism may in fact determine the structure of both.

Before beginning the comparison with experiment outlined above, we remark that

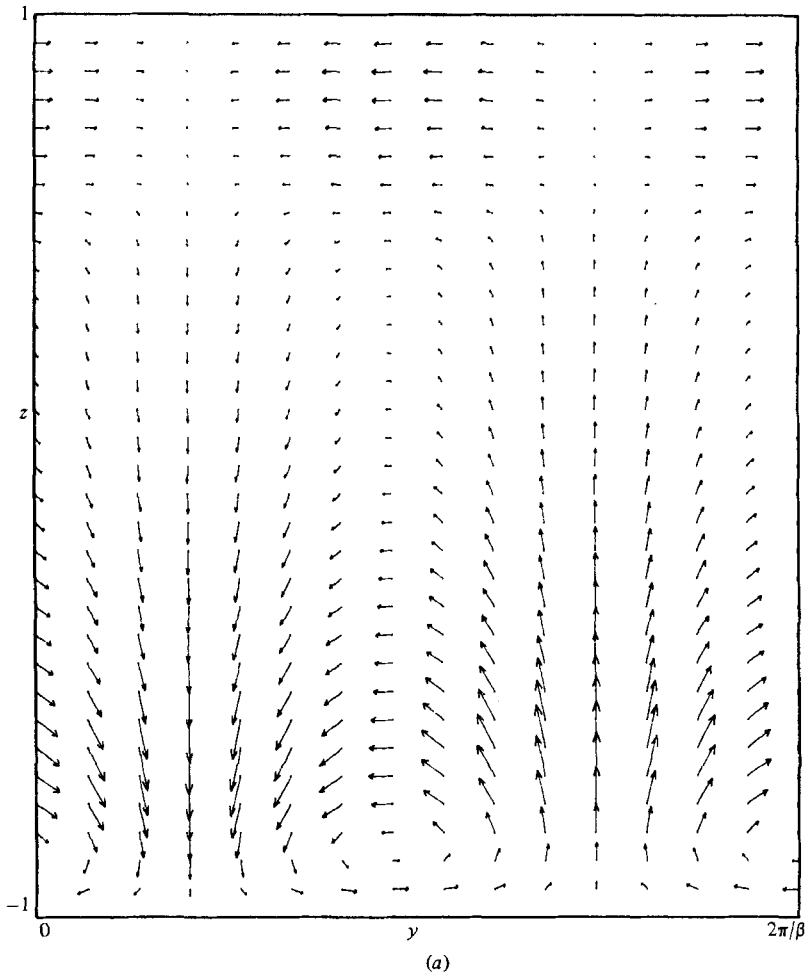


FIGURE 21(a). For caption see facing page.

the instability is intrinsically three-dimensional and occurs on a fast (convective) timescale, two features which strongly mark actual shear-flow transition but which are absent from many models.

With respect to (i), the single most important parameter governing transition is of course the Reynolds number. The critical Reynolds numbers predicted by the secondary instability for plane Poiseuille flow (figures 4 and 5), pipe flow (figure 11) and plane Couette flow (figure 19) are 1000, 1000–3000 and 1000 respectively, which are in good agreement with the Reynolds numbers at which typical (noisy) flows undergo transition. Note that our theory, which requires an appreciable two-dimensional disturbance, does not address the early stages of transition in a careful experiment, with very low background disturbances, although it is believed that in the later stages the secondary instability presented here will again become important. In fact, the existence of a threshold two-dimensional amplitude (figure 7) perhaps explains why careful experiments can sometimes achieve laminar flows at relatively high Reynolds numbers (Nishioka *et al.* 1975; Pfenninger 1961) – if in the test section initially very small (two-dimensional) perturbations cannot achieve the threshold

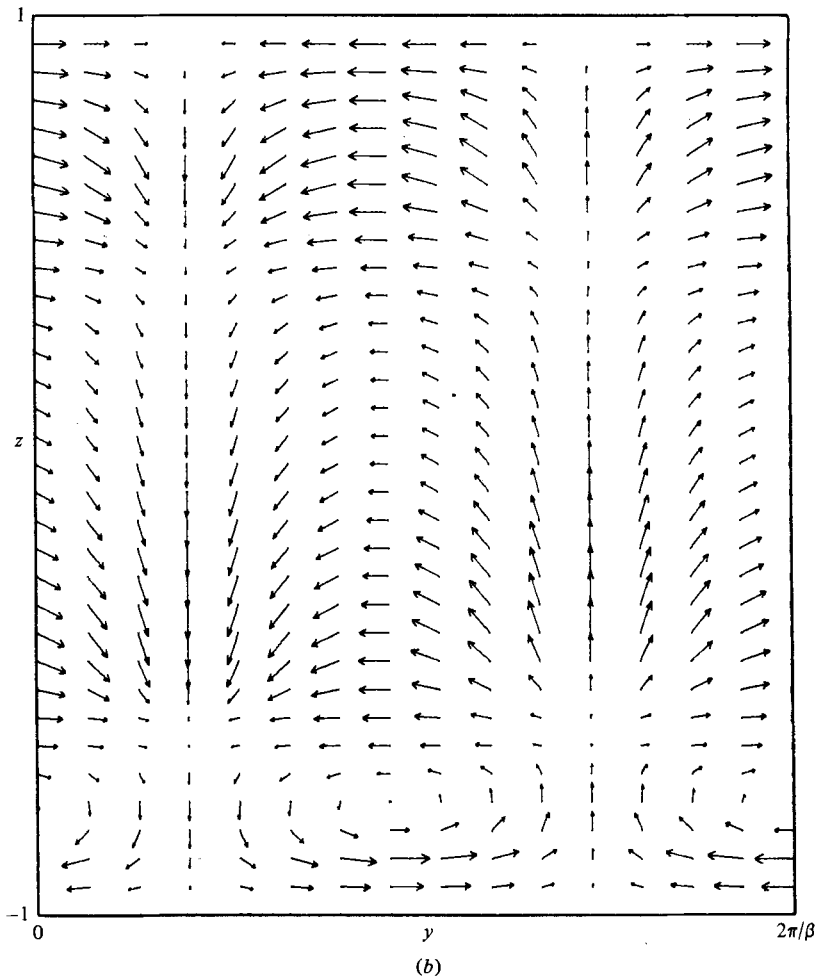


FIGURE 21. Projection of $\mathbf{v}^{(3)}$ on the (y, z) -plane at two streamwise locations within the region of large excitation (cf. figure 15). The plot in (a) is made at a distance $2\pi/16\alpha$ upstream from that given in (b). The vortex structure is deduced from these plots to be inclined at an angle of roughly 16° with respect to the wall.

amplitude required for three-dimensional growth, transition does not occur. This argument requires slow growth of two-dimensional disturbances, which is consistent with the analysis in §3.

The above argument suggests that it should be easier to maintain laminar pipe flow at high Reynolds numbers than laminar plane Poiseuille given the apparent lack of two-dimensional equilibria in the former; and in fact this is found experimentally. The lack of equilibria in pipe flow may also be related to the intermittency found in that flow (for an example of how this may occur in a low-order dynamical system see Manneville & Pomeau 1980). Forcing the axisymmetric component of pipe flow (figures 10 and 11) separates the intermittency effects from those driving three-dimensional transitions.

Next, question (ii) is addressed, i.e. how well the model predicts (in the case of plane Poiseuille flow) the structure and dynamics of turbulent spots. Earlier, theoretical work on this question in the context of boundary layers is surveyed by Craik (1980),

with particular attention to the Benney & Lin (1960) weakly nonlinear model. A schematic picture of a turbulent spot (Carlson *et al.* 1981) at $R = 1000$ is given in figure 20. The features to be explained are the spacing and width of the streaks, denoted \bar{y} and Δy respectively, the spreading angle θ , the advancing angle ϕ and the velocities of the front and rear of the disturbance, v_f and v_r respectively. The photographs from which figure 20 is deduced are obtained in visualization experiments using mica flakes – structures in figure 20 correspond to shears sufficiently large to align the platelets.

A reasonable prediction for \bar{y} and Δy on the basis of secondary instability is

$$\bar{y} = \frac{2\pi}{\beta_{\text{opt}}}, \quad \frac{\Delta y}{\bar{y}} \sim \frac{\beta_{\text{opt}}}{\Delta\beta}, \quad (7.1), (7.2)$$

where β_{opt} is that spanwise wavenumber which maximizes the growth rate σ , and $\Delta\beta$ is the ‘half-width’ of the $\sigma(\beta)$ curve. From figure 2 (or 3) (taking α_{opt} to be of the order of 1.25–1.50 from figure 6) then $\beta_{\text{opt}} \approx 2$ and $\Delta\beta \approx 8 \gg 1$, from which it follows that $\bar{y} \approx 3.1$ (non-dimensionalized with respect to channel half-width) and $\Delta y/\bar{y} \approx 0.25 \ll 1$. These compare favourably with the experimental results, $\bar{y} = 3.8$, $\Delta y/\bar{y} \approx 0.2$. (Note that $\Delta y/\bar{y}$ is a measure of the streakiness of the flow.)

The secondary instability mechanism can be used to predict relationships between v_f and θ . If it is assumed that the front of the spot is quasi-two-dimensional, then as the spanwise tips of the spot proceed downstream one can think of a (finite-amplitude) two-dimensional flow advancing into quiescent fluid. Near the spanwise tips (located at, say, $x = 0$, $y = 0$ at $t = 0$), we write

$$A \sim f(x - v_f t) \left(1 - \frac{2y}{\bar{y}} + \dots \right) e^{\sigma t}, \quad (7.3)$$

where A is any three-dimensional quantity, say the maximum stress. Travelling with the tip (assuming three-dimensional quantities remain small and hence do not affect the two-dimensional packet), $t = x/v_f$, so that

$$A \sim f(0) \left(1 - \frac{2y}{\bar{y}} + \dots \right) e^{\sigma x/v_f}. \quad (7.4)$$

To find the spreading angle we linearize around $x = 0$, $y = 0$, finding dy/dx holding A constant, i.e. the rays are determined for which a constant threshold shear is maintained given that as the instability ‘spreads’ in y it is swept downstream. We assume that the three-dimensional and two-dimensional packets travel at the same speed on the basis that the corresponding infinite wavetrains do so (cf. (4.2)). Performing the calculation, it follows that

$$\left. \left(\frac{\partial y}{\partial x} \right) \right|_{A, x, y=0} = \frac{|\partial A/\partial x|}{|\partial A/\partial y|} = \frac{\sigma \bar{y}}{2v_f}, \quad (7.5)$$

so

$$\tan \theta \approx \frac{\sigma \bar{y}}{2v_f}. \quad (7.6)$$

From figure 5 we take σ at $R = 1000$ to be 0.07. From the experiments v_f is about 0.6, and $\bar{y} \approx 3$. Inserting these quantities into (7.6) gives $\theta \approx 10^\circ$, in good agreement with the experimental value of 8° . It should be noted that the above argument of spreading by destabilization does not explicitly require exponential growth (owing to the linearization (7.5)). However, the speed with which the instability grows to

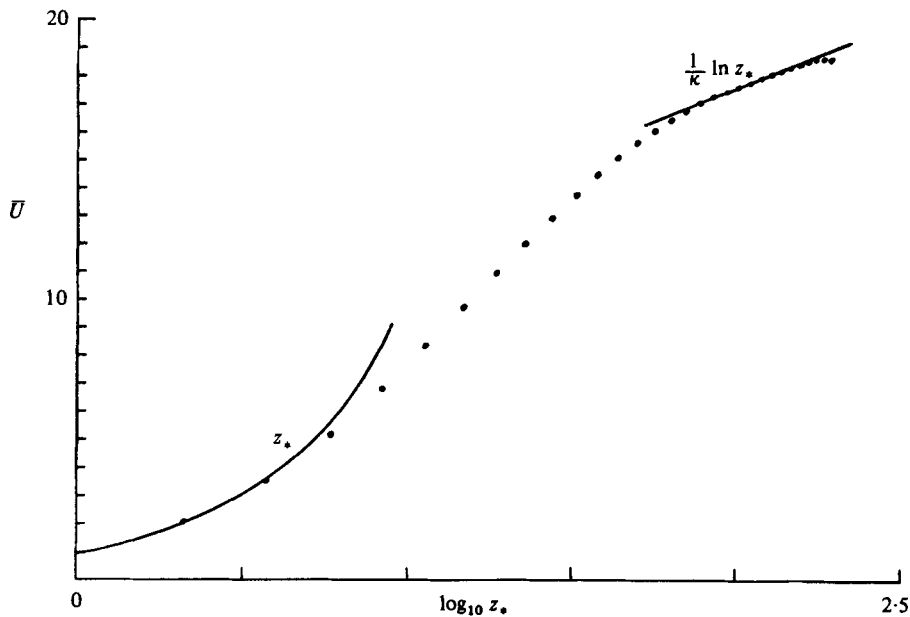


FIGURE 22. Mean turbulent profile obtained in direct numerical simulation of plane Poiseuille flow at $R = 5000$, $\alpha = \beta = 1.32$. Note the viscous sublayer, buffer region, and logarithmic layer of 8–9 data points (with von Kármán constant of about 0.46).

large amplitude (as seen by the streaks remaining behind the front) do suggest an exponential mechanism.

Another feature of the secondary instability reminiscent of actual turbulent shear flows is the vortical structure near the region of excitation (cf. figure 15). In figure 21 we plot projections of the velocity field on (y, z) -planes at two streamwise locations within the (narrow) excitation region of $\mathbf{v}^{(3)}$. There is a longitudinal (streamwise) vortex located *near* the wall inclined at an angle of roughly 16° , indicating a possible relation between our secondary instability and the hairpin vortices inclined at 13° – 18° to the wall observed experimentally (Rajagopalan & Antonia 1979, Brown & Thomas 1977).

The last remaining issue (iii) determines whether the secondary instability presented here saturates in an ordered tertiary state when it reaches finite amplitude, or whether it results in chaotic behaviour. On the basis of large numerical simulation (Orszag & Patera 1981*b*), we have demonstrated that if a tertiary state exists it is unstable. It was found that, starting from initial conditions of the form (4.1) but now with $\epsilon = O(1)$ rather than infinitesimal (and using correspondingly higher spatial resolution to accurately calculate the nonlinear interactions) the flow rapidly develops the characteristics normally associated with turbulent channel flow. In particular, although significant fluctuations are present in the streamwise velocity from horizontal position to horizontal position, averaging over horizontal planes gives a mean profile (plotted in wall coordinates in figure 22) in good agreement with experiment.

We would like to thank Drs T. H. Herbert, W. V. R. Malkus and P. S. Marcus for helpful comments and discussions. This work was supported by the Office of Naval Research under Contracts N00014-77-C-0138 and N00014-79-C-0478, the National Science Foundation under Grant No. ATM-8017284, and NASA Langley Research

Center under Contract NAS1-16722. The computations were performed at the Computing Facility of the National Center for Atmospheric Research, which is supported by the National Science Foundation.

Appendix I. Numerical solution of (4.5)–(4.8)

The eigenvalue problem given by (4.5)–(4.8) is solved using spectral methods (Gottlieb & Orszag 1977). The solution of a problem by such methods involves three steps. First, an appropriate spectral expansion must be chosen. Secondly, a projection operator must be used to project the (infinite-) dimensional solution onto the finite-dimensional (truncated) spectral expansion. Thirdly, the matrix equation generated in the previous step (i.e. the discretized differential equation) must be inverted.

In this paper we deal almost exclusively with flows that are periodic in the x (streamwise) and y (spanwise) directions and bounded by walls at $z = \pm 1$. In the periodic directions Fourier modes are the natural (and appropriate) expansion. Besides providing rapid numerical convergence, they are ideally suited for modal analysis (i.e. only one mode $e^{i\beta my}$ is retained in (4.3)). In the z -direction Fourier expansions are no longer optimal. In particular, an expansion should be used that converges faster than algebraically (with n) independent of any special conditions at the boundaries. An expansion based on the (complete) set of eigenfunctions of a singular Sturm–Liouville problem will in fact satisfy this criterion. (Fourier modes, which are associated with a regular Sturm–Liouville problem, will not.) A particularly good choice is a Chebyshev-polynomial expansion:

$$\mathbf{v} = \sum_{p=0}^P \sum_{n=-N}^N \sum_{m=-M}^M \mathbf{v}_{nmp}(t) e^{i\alpha nx} e^{i\beta my} T_p(z). \quad (\text{A } 1.1)$$

Here T_p is the p th Chebyshev polynomial defined by

$$T_p(\cos \theta) = \cos p\theta. \quad (\text{A } 1.2)$$

The fact that Chebyshev-polynomial expansions of smooth functions converge faster than algebraically can be demonstrated by noting that $f(z) = \sum a_n T_n(z)$ implies that

$$f(\cos \theta) \equiv h(\theta) = \sum a_n \cos n\theta. \quad (\text{A } 1.3)$$

Here h is a periodic even function of θ , from which it follows that $a_n = O(n^{-p})$ as $n \rightarrow \infty$ if f is C_p .

Chebyshev polynomials are especially attractive when considering flow near a wall (where boundary layers form) in that the resolution (i.e. the spacing of the collocation points) goes like $1/P^2$ near $z = \pm 1$. To resolve a boundary layer of thickness δ requires only $\delta^{-\frac{1}{2}}$ polynomials (Gottlieb & Orszag 1977).

The eigenvalue calculation of (4.5)–(4.8) is typically done with $P = 32$, $N = M = 1$. The convergence of the results in P has been checked by comparing results obtained with $P = 16$ and $P = 32$. The convergence in N has been verified using a full simulation (with N typically 8). Equations (4.5)–(4.8) are discretized using a Galerkin procedure in x (and y) and a collocation (pseudospectral) method in z . In the z -direction, the collocation equations at the wall are replaced with the boundary conditions (2.4).

The actual rank of the matrix is reduced by about a factor of 8 due to the three symmetries (4.10)–(4.12). In practice, not all four equations (4.5)–(4.8) need be solved; after setting up all four equations, it is possible to eliminate v_{nm} and ζ_{nm} algebraically.

The algebraic eigenvalue problem is solved using either a global (QR) algorithm, or a local inverse Rayleigh iteration.

Note that in (4.5)–(4.8) (\bar{U}, \bar{W}) is assumed known. The mean flow (\bar{U}, \bar{W}) (and the phase speed c) are calculated in a very similar fashion as $(\mathbf{v}_{nm}^{(3)}, \sigma)$ in (4.5)–(4.8). Global methods can no longer be applied (since the problem is nonlinear in (\bar{U}, \bar{W})). However, a Newton iteration still provides rapid convergence. The calculation of the two-dimensional equilibria is reported by Herbert (1976) and Orszag & Patera (1981*a*).

Appendix II. Direct numerical solution of planar shear flows

We have already discussed spectral expansions appropriate for the solution of wall-bounded flows in appendix I. In this appendix, we consider time-stepping procedures and the required operator inversions in direct numerical solutions of planar shear flows. As indicated previously, the velocity is expanded as

$$\mathbf{v} = \sum_{p=0}^P \sum_{n=-N}^N \sum_{m=-M}^M \mathbf{v}_{nmp}(t) e^{i\alpha n x} e^{i\beta m y} T_p(z), \tag{A 2.1}$$

where the T_p are the Chebyshev polynomials. Here \mathbf{v} satisfies the Navier–Stokes equations

$$\frac{\partial \mathbf{v}}{\partial t} = \mathbf{v} \times \boldsymbol{\omega} - \nabla \pi + \frac{1}{R} \nabla^2 \mathbf{v} + f \hat{\mathbf{x}}, \tag{A 2.2}$$

$$\nabla \cdot \mathbf{v} = 0 \tag{A 2.3}$$

with the boundary conditions

$$\mathbf{v}(x, y, z = \pm 1, t) = 0, \tag{A 2.4}$$

where f is a general forcing term ($2/R$ in the case of plane Poiseuille flow), $\boldsymbol{\omega} = \nabla \times \mathbf{v}$, and π is the pressure head.

There are two distinct time-stepping procedures that we have used. The first, called a fractional-step (or splitting) technique, imposes incompressibility and the viscous boundary conditions in different fractional time steps. Because the pressure and viscous operators do not commute when rigid boundary conditions are imposed, an additional time-stepping error is incurred (Orszag & Kells 1980). The time-stepping procedure is given by

$$\frac{\hat{\mathbf{v}}^{q+1} - \mathbf{v}^q}{\Delta t} = \frac{3}{2}(\mathbf{v} \times \boldsymbol{\omega})^q - \frac{1}{2}(\mathbf{v} \times \boldsymbol{\omega})^{q-1} + f \hat{\mathbf{x}}, \tag{A 2.5}$$

$$\frac{\hat{\hat{\mathbf{v}}}^{q+1} - \hat{\mathbf{v}}^{q+1}}{\Delta t} = -\nabla \pi, \quad \nabla \cdot \hat{\hat{\mathbf{v}}}^{q+1} = 0, \tag{A 2.6}$$

$$\hat{\hat{w}}^{q+1}(x, y, z = \pm 1) = 0,$$

$$\frac{\mathbf{v}^{q+1} - \hat{\hat{\mathbf{v}}}^{q+1}}{\Delta t} = \frac{1}{R} \nabla^2 \mathbf{v}^{q+1}, \quad \mathbf{v}^{q+1}(x, y, z = \pm 1) = 0, \tag{A 2.7}$$

where a superscript q refers to time step. The first step (A 2.5) incorporates the nonlinear effects. With collocation, it requires only order $N^3 \log_2 N$ operations using the fast Fourier transform (which also applies to Chebyshev-polynomial transforms viewed as cosine transforms), where N here represents the typical resolution in one of the directions. This should be contrasted with the operation count of order N^6 if a direct Galerkin procedure (not based on transform methods) were used. The time-stepping procedure used in (A 2.5) is an Adams–Bashforth explicit scheme, which incurs errors of $O(\Delta t^2)$.

The second step, (A 2.6), imposes incompressibility. The vector equations can be reduced to a Poisson equation for the cross-stream velocity, which is solved subject to the inviscid boundary conditions (i.e. $\hat{w} = 0$ at $z = \pm 1$). At the end of this step, the flow is incompressible, but the viscous boundary conditions are not satisfied.

The last step, (A 2.7), incorporates the viscous effects and imposes the viscous boundary conditions. The time-stepping scheme (Euler backward) is only first order, the benefit of a second-order scheme being reduced because of the splitting errors. There is no time-step restriction on this step as the scheme is implicit. The overall error can be reduced to $O(\Delta t^2)$ or smaller by local Richardson extrapolation methods.

The remaining point to be discussed is the discretization and inversion of the Poisson equations in (A 2.6) and (A 2.7). In general, a Galerkin method is used in x and y . In z , either a tau method (Gottlieb & Orszag 1977) or a collocation-diagonalization method is used. The former results in a tridiagonal matrix which can be efficiently inverted (Orszag & Kells 1980; Gottlieb & Orszag 1977) in $O(NMP)$ operations, whereas the latter involves diagonalizing a full matrix and requires $O(NMP^2)$ operations to invert the matrix (Patera & Orszag 1981). With $P = 33$, $N = 16$, $M = 16$, a (vectorized) code using the tridiagonal method requires about 0.4 s on the Cray-1 computer, whereas the same resolution code with the diagonalization method runs roughly three times slower. Collocation-diagonalization becomes more attractive when considering non-constant-coefficient equations (see appendices III and V).

The second time-stepping procedure we have used may be called a full-step method. Here we combine the two steps (A 2.6) and (A 2.7) into one step

$$\frac{u^{q+1} - \hat{u}^{q+1}}{\Delta t} = -i\alpha\pi + \frac{1}{R} \nabla^2 \left(\frac{u^{q+1} + u^q}{2} \right), \quad (\text{A 2.8})$$

$$\frac{v^{q+1} - \hat{v}^{q+1}}{\Delta t} = -i\beta\pi + \frac{1}{R} \nabla^2 \left(\frac{v^{q+1} + v^q}{2} \right), \quad (\text{A 2.9})$$

$$\frac{w^{q+1} - \hat{w}^{q+1}}{\Delta t} = -D\pi + \frac{1}{R} \nabla^2 \left(\frac{w^{q+1} + w^q}{2} \right), \quad (\text{A 2.10})$$

$$i\alpha u^{q+1} + i\beta v^{q+1} + Dw^{q+1} = 0, \quad (\text{A 2.11})$$

$$u^{q+1} = v^{q+1} = w^{q+1} = 0 \quad (z = \pm 1), \quad (\text{A 2.12})$$

where u , v and w are the streamwise, spanwise and cross-stream velocities respectively. (We are considering here one typical Fourier mode, say $n = m = 1$, as (A 2.8)–(A 2.12) are linear and hence modes do not mix. We drop the subscripts n , m for convenience.) Note that (A 2.8)–(A 2.12) is now second order in Δt (in contrast to the splitting method). We can reduce the system (A 2.8)–(A 2.12) to a single fourth-order equation for $w \equiv w^{q+1}$ by taking $D(i\alpha(A 2.8) + i\beta(A 2.9))$, eliminating u , v via (A 2.11), and adding this to $(k^2(A 2.10))$, where $k^2 = \alpha^2 + \beta^2$. The resulting equation is

$$\frac{1}{R} (D^2 - k^2)^2 w - \frac{2}{\Delta t} (D^2 - k^2) w = g \quad (\text{A 2.13})$$

with boundary conditions

$$w = Dw = 0 \quad (z = \pm 1). \quad (\text{A 2.14})$$

Here g represents the inhomogeneous terms involving \hat{v}^{q+1} , \hat{v}^q . (Upon solution of (A 2.13)–(A 2.14), u and v can then be inferred from incompressibility and the

cross-stream vorticity equation.) Equation (A 2.13) is best solved by decoupling it into two second-order equations

$$(D^2 - k^2)w = \zeta, \tag{A 2.15}$$

$$\left(D^2 - k^2 - \frac{2}{\Delta t}\right)\zeta = g, \tag{A 2.16}$$

after which the solution techniques described above (i.e. tridiagonal or diagonalization solution) apply directly. (One subtlety should be pointed out. Only one boundary condition, $w = 0$, can be applied directly to (A 2.15)–(A 2.16). The other should be applied using a Green-function technique to determine the appropriate non-homogeneous boundary conditions on ζ such that $Dw = 0$ at $z = \pm 1$.)

Both the splitting and full time-stepping methods outlined above have been used to verify the results presented in this paper. Additional accuracy checks come from the agreement between the direct simulation results and the eigenvalue results. The codes have also been checked against known results (such as those of linear theory). Typical parameter values for the secondary instability calculations are $P = 33$, $N = 8$, $M = 1$, $\Delta t = 0.025$. Convergence in all these parameters has been verified by either halving or doubling the resolution. The turbulent simulation results presented in figure 22 derive from a run made with $P = 65$, $N = M = 32$ (Orszag & Patera 1981*b*).

Appendix III. Numerical simulations of pipe flow

Pipe-flow simulations differ from planar-flow simulations in three principal ways. First, the Poisson operators no longer have constant coefficients. Secondly, the vector Laplacian (in the viscous term) is no longer diagonal. Lastly, there is a singularity in the coordinate system at $r = 0$. Except for modifications to accommodate these difficulties, pipe-flow simulations proceed very much like simulations in planar geometries (see appendix II).

The effect of non-constant-coefficient Poisson operators is to make collocation-diagonalization methods more attractive (*vis-à-vis* tau techniques). The more complicated equations in cylindrical geometry also preclude the full-step method described in appendix II: the fourth-order equation (A 2.13) no longer exists in the general non-axisymmetric case. Therefore we have used splitting methods for the pipe-flow calculations.

The problem of a non-diagonal vector Laplacian (which would lead to large matrix inversions) is simply solved. The problem is that if

$$\nabla^2 \mathbf{v} = \mathbf{A} \begin{Bmatrix} u_{nm} \\ v_{nm} \\ w_{nm} \end{Bmatrix} e^{inax} e^{im\theta} = \begin{Bmatrix} f_1 \\ f_2 \\ f_3 \end{Bmatrix} e^{inax} e^{im\theta} \tag{A 3.1}$$

then \mathbf{A} is not a diagonal matrix (in contrast with the Cartesian case). Here u_{nm} , v_{nm} and w_{nm} are the axial, azimuthal and radial velocities respectively. Fourier-transformed in x and θ ; for now the r -dependence is kept in physical-space representation. Also, f is an arbitrary inhomogeneous term. The transformation

$$\left. \begin{aligned} \tilde{u}_{nm} &= u_{nm}, & \tilde{f}_1 &= f_1, \\ \tilde{v}_{nm} &= v_{nm} - iw_{nm}, & \tilde{f}_2 &= f_2 - if_3, \\ \tilde{w}_{nm} &= v_{nm} + iw_{nm}, & \tilde{f}_3 &= f_2 + if_3 \end{aligned} \right\} \tag{A 3.2}$$

gives

$$\tilde{\mathbf{A}} \begin{Bmatrix} \tilde{u}_{nm} \\ \tilde{v}_{nm} \\ \tilde{w}_{nm} \end{Bmatrix} = \begin{Bmatrix} \tilde{f}_1 \\ \tilde{f}_2 \\ \tilde{f}_3 \end{Bmatrix}, \quad (\text{A } 3.3)$$

where $\tilde{\mathbf{A}}$ is diagonal. (This diagonalization should not be confused with the (eigenfunction representation) diagonalization of the r -dependence of each element of $\tilde{\mathbf{A}}$ which is done when collocation is used.)

The last point concerns the spectral expansion itself. In a pipe $0 \leq r \leq 1$, while the Chebyshev variable z satisfies $-1 \leq z \leq 1$. The two domains can be made to coincide in one of two ways. First, the Chebyshev variable can be rescaled to cover only the interval $[0, 1]$. This has the disadvantage of crowding many points near $r = 0$, which is not a physical boundary. (Note, however, that linear theory predicts centre modes that are concentrated near the origin; for good resolution of these modes it may in fact be wise to rescale.) The other option is to expand the velocities in even or odd Chebyshev series, thus maintaining the normal spacing of collocation points at $r = 0$. The parity of the expansion must be chosen to be compatible with the behaviour of the variable at the origin. The leading behaviour of the velocity as $r \rightarrow 0$ (derived from a local analysis of $\tilde{\mathbf{A}}$) gives

$$\tilde{u}_{nm} \sim r^{\pm m} \quad (m > 0); \quad 1, \ln r \quad (m = 0), \quad (\text{A } 3.4)$$

$$\tilde{v}_{nm} \sim r^{\pm(m-1)} \quad (m \neq 1); \quad 1, \ln r \quad (m = 1), \quad (\text{A } 3.5)$$

$$\tilde{w}_{nm} \sim r^{\pm(m+1)} \quad (m \geq 0). \quad (\text{A } 3.6)$$

Thus the appropriate spectral expansion is

$$v_k(x, \theta, r, t) = \sum_{m=-M}^M \sum_{n=-N}^N \sum_{p=0}^P v_{nmp,k}(t) e^{i\alpha n x} e^{i\beta m \theta} T_l(r), \quad (\text{A } 3.7)$$

where $v_1 = u$, $v_2 = v$, $v_3 = w$, $l = 2p + b(k, \beta|m|)$, with

$$b(r, s) = \begin{cases} 0 & (r = 1, s \text{ even}) \quad \text{or} \quad (r = 2, 3, s \text{ odd}), \\ 1 & (r = 1, s \text{ odd}) \quad \text{or} \quad (r = 2, 3, s \text{ even}). \end{cases} \quad (\text{A } 3.8)$$

The pipe-flow code has been tested against linear theory as well as previous nonlinear axisymmetric calculations (Patera & Orszag 1981). Resolution tests have been performed indicating that $P = 32$ (or even 16), $N = 8$ is adequate for resolution of wall modes. Higher resolution (in r) is required for centre modes; rescaling the Chebyshev variable to the interval $0 \leq r \leq 1$ in such cases is probably better than parity-observing expansions on $-1 \leq r \leq 1$.

Appendix IV. Energetics of linear secondary instability

In this appendix we write explicitly the terms appearing in (5.4)–(5.6). The energies $E^{[2]}$ and $E^{[3]}$ are the same as $E^{(2)}$ and $E^{(3)}$ defined previously in (4.4). $E^{[1]}$ is defined as

$$E^{[1]} = \frac{15}{16} \int_{-1}^1 (U'_{\parallel})^2 dz. \quad (\text{A } 4.1)$$

The transfer and dissipation rates are then obtained by taking the scalar product of \mathbf{v}_{-n-m} and $\partial \mathbf{v}_{nm} / \partial t$ and appropriately summing the contributions from the nonlinear and viscous terms. The periodic pressure term conserves energy in each Fourier mode

and hence does not contribute to transfer (although it does transfer energy between velocity components in a given Fourier mode). Therefore

$$T^{12} = \frac{15}{8} \int_{-1}^1 U'_{\parallel} \hat{\mathbf{x}} \cdot \sum_{p=1}^N 2 \operatorname{Re} (\mathbf{v}_p^{(2)} \times \boldsymbol{\omega}_p^{(2)\dagger}) dz, \quad (\text{A } 4.2)$$

$$T^{13} = \frac{15}{8} \epsilon^2 \int_{-1}^1 U'_{\parallel} \hat{\mathbf{x}} \cdot \sum_{q=\pm 1} \sum_{p=0}^N \frac{2}{1 + \delta_{0p}} \operatorname{Re} (\mathbf{v}_{pq}^{(3)} \times \boldsymbol{\omega}_{pq}^{(3)\dagger}) dz, \quad (\text{A } 4.3)$$

$$T^{23} = -T^{13} + \frac{15}{8} \epsilon^2 \int_{-1}^1 \sum_{q=\pm 1} \sum_{p=0}^N \frac{2}{1 + \delta_{0p}} \operatorname{Re} (\mathbf{v}_{pq}^{(3)} \cdot (\mathbf{v} \times \boldsymbol{\omega})_{pq}^{(3)\dagger}) dz, \quad (\text{A } 4.4)$$

and

$$D^{[1]} = \frac{15}{8} \int_{-1}^1 \frac{U'_{\parallel}}{R} (2 + \nabla^2 U'_{\parallel}) dz, \quad (\text{A } 4.5)$$

$$D^{[2]} = \frac{15}{8} \int_{-1}^1 \sum_{p=1}^N 2 \operatorname{Re} (\mathbf{v}_p^{(2)\dagger} \cdot \nabla^2 \mathbf{v}_p^{(2)}) dz, \quad (\text{A } 4.6)$$

$$D^{[3]} = \epsilon^2 \frac{15}{8} \int_{-1}^1 \sum_{q=\pm 1} \sum_{p=0}^N \frac{2}{1 + \delta_{0p}} \operatorname{Re} (\mathbf{v}_{pq}^{(3)\dagger} \cdot \nabla^2 \mathbf{v}_{pq}^{(3)}) dz. \quad (\text{A } 4.7)$$

Here $\boldsymbol{\omega} = \nabla \times \mathbf{v}$ and $(\mathbf{v} \times \boldsymbol{\omega})^{(3)} = \mathbf{v}^{(2)} \times \boldsymbol{\omega}^{(3)} + \mathbf{v}^{(3)} \times \boldsymbol{\omega}^{(2)}$. Note that the flow work done by the constant pressure gradient is included in $D^{[1]}$. We also define the normalized quantities

$$\bar{T}^{13} = \frac{T^{13}}{E^{[3]}}, \quad \bar{T}^{23} = \frac{T^{23}}{E^{[3]}}, \quad \bar{D}^{[3]} = \frac{D^3}{E^{[3]}}, \quad (\text{A } 4.8)$$

so that

$$2\sigma = \bar{T}^{13} + \bar{T}^{23} + \bar{D}^{[3]}, \quad (\text{A } 4.9)$$

where σ is the growth of the three-dimensional amplitude.

Appendix V. Numerical simulations of boundary layers

Boundary-layer simulations (with periodic x - and y -dependence) are identical with channel simulations except that the semi-infinite $[0, \infty]$ physical domain must be mapped into the $[-1, 1]$ Chebyshev-polynomial domain. This implies that collocation should be used since the mapping introduces (non-trivial) non-constant coefficients into the Laplacian. The only point we will discuss here is the choice of mapping.

Besides the technical requirement that $z = 0$ in physical space map into $\eta = -1$ in Chebyshev space, and that $z = \infty$ map into $\eta = 1$ we also require good resolution within the boundary layer at the expense of resolution in the free stream. A mapping that works quite well in practice is

$$z = \frac{\gamma(1+\eta)}{1-\eta} \quad (-1 \leq \eta < 1). \quad (\text{A } 5.1)$$

With this mapping half of the collocation points satisfy $z < \gamma$, and half satisfy $z > \gamma$. The results presented in this work were obtained with $\gamma = 1.875$ (roughly the displacement thickness).

The effect of the mapping (A 5.1) is to transform $\partial/\partial z$ into

$$\frac{\partial}{\partial z} = \frac{\partial \eta}{\partial z} \frac{\partial}{\partial \eta} = \frac{(1-\eta)^2}{2\gamma} \frac{\partial}{\partial \eta}. \quad (\text{A } 5.2)$$

Derivatives can still be obtained in order $P \log_2 P$ operations (with P the number of Chebyshev polynomials in the expansion), if $\partial/\partial\eta$ is evaluated using transform methods while the multiplication by $\partial\eta/\partial z$ is done in physical space.

REFERENCES

- BENNEY, D. J. & LIN, C. C. 1960 On the secondary motion induced by oscillation in a shear flow. *Phys. Fluids* **3**, 656.
- BRACHET, M. & ORSZAG, S. A. 1983 Secondary instability of free-shear flows. (To be published.)
- BROWN, G. L. & THOMAS, A. S. W. 1977 Large structure in a turbulent boundary layer. *Phys. Fluids Suppl.* **20**, S243.
- BUSSE, F. H. 1969 Bounds on the transport of mass and momentum by turbulent flow between parallel plates. *Z. angew. Math. Phys.* **20**, 1.
- CARLSON, D., WIDNALL, S. E. & PEETERS, M. F. 1981 A flow visualization study of transition in plane Poiseuille flow. *Flow Dynamics Research Lab. (Dept of Aero, and Astro., M.I.T.) Rep.* no. 81-3.
- CLEVER, R. M. & BUSSE, F. H. 1974 Transition to time-dependent convection. *J. Fluid Mech.* **65**, 625.
- CRAIK, A. D. D. 1980 Nonlinear evolution and breakdown in unstable boundary layers. *J. Fluid Mech.* **99**, 247.
- DAVEY, A. 1973 On the stability of plane Couette flow to infinitesimal disturbances. *J. Fluid Mech.* **57**, 689.
- DAVEY, A. & DRAZIN, P. G. 1969 The stability of Poiseuille flow in a pipe. *J. Fluid Mech.* **36**, 209.
- DAVEY, A. & NGUYEN, H. P. F. 1971 Finite-amplitude stability of pipe flow. *J. Fluid Mech.* **45**, 701.
- DRAZIN, P. G. & REID, W. H. 1981 *Hydrodynamic Stability*. Cambridge University Press.
- ELLINGSON, T. & PALM, E. 1975 Stability of linear flow. *Phys. Fluids* **18**, 487.
- FEIGENBAUM, M. 1980 The transition to aperiodic behavior in turbulent systems. *Commun. Math. Phys.* **77**, 65.
- GOLLUB, J. P. & BENSON, S. H. 1980 Many routes to turbulent convection. *J. Fluid Mech.* **100**, 449.
- GORMAN, M., REITH, L. A. & SWINNEY, H. L. 1980 Moderation patterns, multiple frequencies, and other phenomena in circular Couette flow. *Ann. N.Y. Acad. Sci.* **357**, 10.
- GÖRTLER, H. & WITTING, H. 1958 Theorie der sekundären Instabilität der laminaren Grenzschichten. In *Proc. IUTAM Symp. Boundary Layer Research* (ed. H. Görtler), p. 110. Berlin.
- GROHNE, D. 1969 Die Stabilität der ebenen Kanalströmung gegenüber dreidimensionalen Störungen von endlicher Amplitude. *A.V.A. Göttingen Rep.* 69-A-30.
- HERBERT, T. 1976 Periodic secondary motions in a plane channel. In *Proc. 5th Int. Conf. on Numerical Methods in Fluid Dynamics* (ed. A. I. Van de Vooren & P. J. Zandbergen). Lecture Notes in Physics, vol. 59, p. 235. Springer.
- HERBERT, T. 1977 Finite amplitude stability of plane parallel flows. *AGARD Conf. Proc.* CP-224, p. 3/1.
- ITOH, N. 1977 Nonlinear stability of parallel flows with subcritical Reynolds numbers. Part 2. Stability of pipe Poiseuille flow to finite axisymmetric disturbances. *J. Fluid Mech.* **82**, 469.
- KLEBANOFF, P. S., TIDSTROM, K. D. & SARGENT, L. M. 1962 The three-dimensional nature of boundary-layer instability. *J. Fluid Mech.* **12**, 1.
- KLEISER, L. & SCHUMANN, U. 1983 Laminar-turbulent transition process in plane Poiseuille flow. In *Proc. Symp. on Spectral Methods*. SIAM.
- LANDAHL, M. T. 1980 A note on an algebraic instability of inviscid parallel shear flows. *J. Fluid Mech.* **98**, 243.
- LIN, C. C. 1955 *The Theory of Hydrodynamic Stability*. Cambridge University Press.
- MANNEVILLE, P. & POMEAU, Y. 1980 Different ways to turbulence in dissipative dynamic systems. *Physica D1*, 219.
- McLAUGHLIN, J. B. & ORSZAG, S. A. 1982 Transition from periodic to chaotic thermal convection. *J. Fluid Mech.* **122**, 123.

- METCALFE, R. W. & ORSZAG, S. A. 1973 Numerical calculation of the linear stability of pipe flows. *Flow Research Rep.* no. 25, Kent, Washington.
- NISHIOKA, M., IIDA, S. & ICHIKAWA, Y. 1975 An experimental investigation of the stability of plane Poiseuille flow. *J. Fluid Mech.* **72**, 731.
- NISHIOKA, M., IIDA, S. & KANBAYASHI, S. 1978 An experimental investigation of the subcritical instability in plane Poiseuille flow. In *Proc. 10th Turbulence Symp. Inst. Space Aero. Sci., Tokyo Univ.*, p. 55.
- ORSZAG, S. A. 1971 Accurate solution of the Orr–Sommerfeld stability equation. *J. Fluid Mech.* **50**, 689.
- ORSZAG, S. A. 1976 Turbulence and transition: a progress report. In *Proc. 5th Int. Conf. on Numerical Methods in Fluid Dynamics* (ed. A. van de Vooren & P. J. Zandbergen). Lecture Notes in Physics, vol. 59, p. 32.
- ORSZAG, S. A. & KELLS, L. C. 1980 Transition to turbulence in plane Poiseuille flow and plane Couette flow. *J. Fluid Mech.* **96**, 159.
- ORSZAG, S. A. & PATERA, A. T. 1980 Subcritical transition to turbulence in plane channel flows. *Phys. Rev. Lett.* **45**, 989.
- ORSZAG, S. A. & PATERA, A. T. 1981*a* Subcritical transition to turbulence in planar shear flows. In *Transition and Turbulence* (ed. R. E. Meyer), p. 127. Academic.
- ORSZAG, S. A. & PATERA, A. T. 1981*b* Calculation of von Kármán's constant for turbulent channel flow. *Phys. Rev. Lett.* **47**, 832.
- PATERA, A. T. & ORSZAG, S. A. 1981 Finite-amplitude stability of axisymmetric pipe flow. *J. Fluid Mech.* **112**, 467.
- PFENNIGER, W. 1961 *Boundary Layers and Flow Control*, vol. 2 (ed. C. V. Leschmann), p. 190. Pergamon.
- PIERREHUMBERT, R. T. & WIDNALL, S. E. 1982 The two- and three-dimensional instabilities of a spatially periodic shear layer. *J. Fluid Mech.* **114**, 59.
- RAJAGOPALAN, S. & ANTONIA, R. A. 1979 Some properties of the large structure in a fully developed turbulent duct flow. *Phys. Fluids* **22**, 614.
- RUELLE, D. & TAKENS, F. 1971 On the nature of turbulence. *Commun. Math. Phys.* **20**, 167.
- SALWEN, H., COTTON, F. W. & GROSCH, C. E. 1980 Linear stability of Poiseuille flow in a circular pipe. *J. Fluid Mech.* **98**, 273.
- SQUIRES, H. B. 1933 On the stability of the three-dimensional disturbances of viscous flow between parallel walls. *Proc. R. Soc. Lond. A* **142**, 621.
- STUART, J. T. 1960 On the non-linear mechanics of wave disturbances in stable and unstable parallel flows. Part 1. The basic behaviour in plane Poiseuille flow. *J. Fluid Mech.* **9**, 11.
- STUART, J. T. 1965 The production of intense shear layers by vortex stretching and convection. *AGARD Rep.* 514.
- WRAY, A. & HUSSAINI, M. Y. H. 1980 Numerical experiments in boundary layer stability. *AIAA Paper* 80-0275.